Nonhydrostatic Modeling of Tsunamis from Earthquake Rupture to Coastal Impact

Yoshiki Yamazaki[1]; Yefei Bai[2]; Linyan Li Goo[3]; Kwok Fai Cheung[4]; and Thorne Lay[5]

Abstract: The last decade has seen the rapid emergence of nonhydrostatic modeling as an advanced tool for studies of tsunami processes and source mechanisms that warrants a critical assessment of the state of the art and value-added features in relation to contemporary approaches. Inclusion of depth-averaged vertical velocity and nonhydrostatic pressure in the nonlinear shallow-water equations enables description of long-wave dynamics in quasi three-dimensional flows. The governing equations involve first-order derivatives, but retain higher-order properties, as in the Boussinesq-type approach. The commonly-used staggered finite difference scheme continues to provide the surface elevation and horizontal velocity, which in turn are updated by the nonhydrostatic pressure evaluated from a Poisson-type equation. In addition to having dispersion properties complementary to the governing equations, the numerical framework allows implementation of time-varying seafloor excitation from earthquake rupture, a shock-capturing scheme for discontinuous flows, and a multilevel two-way nested grid system for dispersive and shock waves. A series of numerical and laboratory benchmarks as well as a case study of the 2011 Tohoku tsunami illustrate the model capabilities in describing tsunami generation, dispersion, shoaling, bore formation, and separation-driven currents with high precision across a wide range of temporal and spatial scales for general application. These capabilities have an important role in resolving effects of detailed earthquake rupture patterns and providing accurate tsunami impact predictions with implications for warning guidance, hazard assessment, and seismological research. **DOI: 10.1061/JHEND8.HYENG-13388.**

Author keywords: Frequency dispersion; Nonhydrostatic models; Shock-capturing schemes; Tsunamis; Tsunami bores; Separation-driven currents.

Introduction

Tsunamis generated by rapid deformation events at subduction zones pose a constant threat to coastal communities around the world. Depth-integrated long-wave models can resolve tsunami processes to varying degree of accuracy, thereby providing a suite of tools for fundamental research and practical application. Nonlinear shallow-water models have been the primary tool with a long record of implementation due to their simple numerical frameworks and low computing costs (e.g., Imamura et al. 1988; Kowalik and Murty 1993a; Liu et al. 1995; Titov and Synolakis 1998; LeVeque et al. 2011). The first-order, hydrostatic governing equations, which were implemented early on for modeling storm surge and astronomical tides, describe flow fields in the horizontal plane with shallow-water celerity independent of the wave period. Although tsunami waves are considered to be weakly dispersive, the slight offset in celerity among harmonic components can accumulate during transoceanic propagation with notable effects to waveforms and coastal impacts (e.g., Bricker et al. 2007; Saito et al. 2010). This has motivated recent implementations of Boussinesq-type or nonhydrostatic models with an initial objective to account for frequency dispersion of tsunami waves.

The Boussinesq-type approach includes vertical flow dynamics in the nonlinear shallow-water equations through higher-order derivatives of the horizontal velocity. Peregrine (1967) attained leading-order dispersion outside the shallow-water range through depth integration of the vertical velocity with a linear profile. The formulation facilitates systematic convergence in deeper water by retaining high-order terms to match the Taylor series expansion of the dispersion relation from Airy wave theory (Madsen et al. 1991; Nwogu 1993; Wei et al. 1995). In a parallel development, Madsen et al. (2003, 2006) extended the formulation to achieve highly accurate dispersion properties with an infinite power-series expansion of the velocity profile. While high-order Boussinesq-type equations have been the mainstay for modeling of wind-generated waves, researchers typically resort to the basic formulation of Peregrine (1967) for weakly dispersive tsunami waves (e.g., Horrillo et al. 2006; Kirby et al. 2013; Saito et al. 2014; Baba et al. 2017). The higher-order derivatives in the governing equations remain a challenge to numerical schemes, especially for two-way grid nesting and wet-dry interface tracking over realistic bathymetry and topography.

An alternative approach for modeling of weakly-dispersive waves is to directly include the vertical velocity and nonhydrostatic

[1]Assistant Researcher, Dept. of Ocean and Resources Engineering, Univ. of Hawaii at Manoa, Honolulu, HI 96822. ORCID: https://orcid.org/0000-0002-2285-9874. Email: yoshikiy@hawaii.edu

[2]Professor, Ocean College, Zhejiang Univ., Zhoushan, Zhejiang 316021, China. ORCID: https://orcid.org/0000-0003-3323-3348. Email: yfbai@zju.edu.cn

[3]Coastal Engineer, Oceanit Inc., 828 Fort St. Mall, Suite 600, Honolulu, HI 96813. Email: lli@oceanit.com

[4]Professor, Dept. of Ocean and Resources Engineering, Univ. of Hawaii at Manoa, Honolulu, HI 96822 (corresponding author). ORCID: https://orcid.org/0000-0002-7435-0500. Email: cheung@hawaii.edu

[5]Professor, Dept. of Earth and Planetary Sciences, Univ. of California, Santa Cruz, CA 95064. ORCID: https://orcid.org/0000-0003-2360-4213. Email: tlay@ucsc.edu

Note. This manuscript was submitted on June 15, 2022; approved on March 10, 2023; published online on July 3, 2023. Discussion period open until December 3, 2023; separate discussions must be submitted for individual papers. This paper is part of the ***Journal of Hydraulic Engineering***, © ASCE, ISSN 0733-9429.

pressure without increasing the order of the governing equations. Yamazaki et al. (2009, 2011a) adapted the depth-integrated Euler equations from Stelling and Zijlema (2003) and the shock-capturing scheme from Stelling and Duinmeijer (2003) in a community model known as NEOWAVE (Non-hydrostatic Evolution of Ocean WAVEs). While the one-layer formulation is sufficient for tsunami modeling, additional layers, instead of higher-order derivatives, can improve linear and nonlinear properties for modeling of wind-generated waves on par with the Boussinesq-type approach (e.g., Zijlema et al. 2011; Smit et al. 2014; Bai et al. 2018). The nonhydrostatic approach can also resolve time-varying kinematic seafloor deformation in concert with finite fault inversion of earthquake rupture as well as the vertical inertia of the subsequent sea-surface descent or upswing, to provide a more complete account of tsunami generation. These features complement the dispersion property in providing an accurate description of tsunami processes for geophysical research and engineering application.

We have been using NEOWAVE to investigate earthquake and tsunami sources, near and far-field wave dynamics, and coastal inundation processes for more than a decade (e.g., Yamazaki et al. 2011b, 2018, 2021; Cheung et al. 2013; Lay et al. 2013; Li et al. 2016a, b; Bai et al. 2017, 2015a, 2022). In addition to event-specific investigations, we have verified the tsunami generation mechanism, participated in model benchmarking studies, and performed mathematical analysis to understand the intrinsic properties of the governing equations and the underlying numeric that influence model prediction (e.g., Bai and Cheung 2013, 2016, 2018; Bai et al. 2015b, 2018; Li and Cheung 2019; Yamazaki et al. 2012). The information is scattered across the technical literature in multiple disciplines, while some of the results were only presented at workshops, meetings or conferences with limited documentation and dissemination. This invited review provides a critical assessment of the mathematical and numerical formulations from experiences gained in model applications as well as previously unpublished verification, benchmarking, and case study results. The assessment aims to provide insights into the state of the art in nonhydrostatic modeling of tsunamis and to highlight the added value in relation to the shallow-water and Boussinesq-type approaches.

Model Description

NEOWAVE is a multifunction code developed for tsunamigenic earthquake research and coastal flood hazard assessment. Its versatility stems from the modular code structure inherent in the governing equations and numerical schemes that allows assembly of model functionalities for specific applications. This section provides a collated summary and a full retrospect of the model formulation from Yamazaki et al. (2009, 2011a) along with theoretical and numerical properties derived by Bai and Cheung (2013, 2018), Bai et al. (2018), and Li and Cheung (2019).

Governing Equations

The nonhydrostatic free-surface flow is defined in a spherical coordinate system with R representing the earth radius and (λ, ϕ, z) the latitude, longitude, and altitude. Fig. 1 provides a schematic of the boundary-value problem, in which ζ and h denote the sea-surface elevation and water depth measured from the still-water level. The elastic half-space solution of Okada (1985) defines the displacement field (ξ_1, ξ_2, ξ_3) from earthquake rupture for projection onto the seafloor. Following Tanioka and Satake (1996), the vertical seafloor displacement is augmented by horizontal motion of the local slope to define the tsunami excitation as

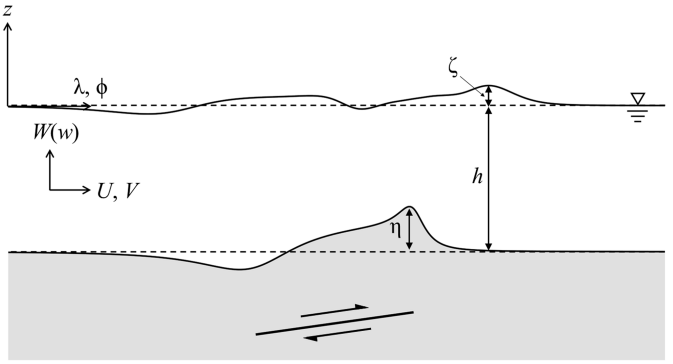

Fig. 1. Schematic of earthquake faulting, seafloor deformation, and free-surface flow in spherical coordinates.

$$\eta = \xi_3 + \frac{\xi_1}{R\cos\phi}\frac{\partial h}{\partial \lambda} + \frac{\xi_2}{R}\frac{\partial h}{\partial \phi} \tag{1}$$

With t denoting time and (U, V) the depth-averaged horizontal velocity, the kinematic free-surface and bottom boundary conditions give the vertical water particle velocity

$$w_s = \frac{\partial \zeta}{\partial t} + \frac{U}{R\cos\phi}\frac{\partial \zeta}{\partial \lambda} + \frac{V}{R}\frac{\partial \zeta}{\partial \phi} \quad \text{at} \quad z = \zeta \tag{2}$$

$$w_b = \frac{\partial \eta}{\partial t} - \frac{U}{R\cos\phi}\frac{\partial (h-\eta)}{\partial \lambda} - \frac{V}{R}\frac{\partial (h-\eta)}{\partial \phi} \quad \text{at} \quad z = -h + \eta \tag{3}$$

The depth-averaged vertical velocity $W = (w_s + w_b)/2$ is computed from a linear profile over the water column consistent with the long-wave approximation. Direct inclusion of the vertical velocity in the formulation allows implementation of the tsunami excitation η in Eq. (3) as time-dependent, forcing to the boundary-value problem. The terms associated with the bottom slopes are generally negligible, but may influence local wave dynamics at shelf breaks, seamounts, and submarine canyons.

Let Ω and g denote the earth angular velocity and gravitational acceleration; ρ the water density; and n the Manning's number for bottom roughness. The evolution of the free-surface flow follows the continuity equation and the momentum equations in the λ, ϕ, and z-directions as

$$\frac{\partial (\zeta - \eta)}{\partial t} + \frac{1}{R\cos\phi}\frac{\partial (UD)}{\partial \lambda} + \frac{1}{R\cos\phi}\frac{\partial (VD\cos\phi)}{\partial \phi} = 0 \tag{4}$$

$$\begin{aligned}
&\frac{\partial U}{\partial t} + \frac{U}{R\cos\phi}\frac{\partial U}{\partial \lambda} + \frac{V}{R}\frac{\partial U}{\partial \phi} - \left(2\,\Omega + \frac{U}{R\cos\phi}\right)V\sin\phi \\
&\quad = -\frac{g}{R\cos\phi}\frac{\partial \zeta}{\partial \lambda} - \frac{1}{\rho R\cos\phi}\frac{\partial Q}{\partial \lambda} - \frac{Q}{\rho DR\cos\phi}\frac{\partial (\zeta - h + \eta)}{\partial \lambda} \\
&\qquad - n^2\frac{g}{D^{1/3}}\frac{U\sqrt{U^2+V^2}}{D}
\end{aligned} \tag{5}$$

$$\begin{aligned}
&\frac{\partial V}{\partial t} + \frac{U}{R\cos\phi}\frac{\partial V}{\partial \lambda} + \frac{V}{R}\frac{\partial V}{\partial \phi} - \left(2\,\Omega + \frac{U}{R\cos\phi}\right)U\sin\phi \\
&\quad = -\frac{g}{R}\frac{\partial \zeta}{\partial \lambda} - \frac{1}{\rho R}\frac{\partial Q}{\partial \phi} - \frac{Q}{\rho DR}\frac{\partial (\zeta - h + \eta)}{\partial \phi} \\
&\qquad - n^2\frac{g}{D^{1/3}}\frac{V\sqrt{U^2+V^2}}{D}
\end{aligned} \tag{6}$$

$$\frac{\partial W}{\partial t} = \frac{2Q}{\rho D} \tag{7}$$

where $D = h + \zeta\text{-}\eta$ is the flow depth; and Q is the depth-averaged non-hydrostatic pressure for an assumed linear profile diminishing to zero at $z = \zeta$ to satisfy the dynamic free-surface boundary condition. For long-wave modeling, the nonlinear advective terms in the vertical momentum equation are small and therefore have been omitted in Eq. (7) for simplicity. There are four governing equations with five unknowns, ζ, U, V, W, and Q. Conservation of mass provides a fifth equation

$$\frac{1}{R\cos\phi}\frac{\partial U}{\partial \lambda} + \frac{1}{R\cos\phi}\frac{\partial (V\cos\phi)}{\partial \phi} + \frac{\partial w}{\partial z} = 0 \tag{8}$$

in which $\partial w/\partial z = (w_s - w_b)/D$ from Eqs. (2) and (3) is a constant over the water column for the linear velocity profile. The equation system, which includes the numerical framework of a one-layer flow, are not completely closed until implementation of the discretization schemes.

The spherical coordinate system (λ, ϕ, z) reduces to the Cartesian system (x, y, z) for modeling of a standalone coastal region or a laboratory experiment as well as mathematical analysis of the governing equations and numerical schemes. Effects of the earth's curvature are negligible and the Coriolis terms in the horizontal momentum equations vanish. The continuity equation and the x, y, and z momentum equations read

$$\frac{\partial(\zeta - \eta)}{\partial t} + \frac{\partial (UD)}{\partial x} + \frac{\partial (VD)}{\partial y} = 0 \tag{9}$$

$$\frac{\partial U}{\partial t} + U\frac{\partial U}{\partial x} + V\frac{\partial U}{\partial y} = -g\frac{\partial \zeta}{\partial x} - \frac{1}{\rho}\frac{\partial Q}{\partial x} - \frac{Q}{\rho D}\frac{\partial(\zeta - h + \eta)}{\partial x} - n^2\frac{g}{D^{1/3}}\frac{U\sqrt{U^2+V^2}}{\rho D} \tag{10}$$

$$\frac{\partial V}{\partial t} + U\frac{\partial V}{\partial x} + V\frac{\partial V}{\partial y} = -g\frac{\partial \zeta}{\partial y} - \frac{1}{\rho}\frac{\partial Q}{\partial y} - \frac{Q}{\rho D}\frac{\partial(\zeta - h + \eta)}{\partial y} - n^2\frac{g}{D^{1/3}}\frac{V\sqrt{U^2+V^2}}{\rho D} \tag{11}$$

$$\frac{\partial W}{\partial t} = \frac{2Q}{\rho D} \tag{12}$$

The conservation of mass becomes

$$\frac{\partial U}{\partial x} + \frac{\partial V}{\partial y} + \frac{\partial w}{\partial z} = 0 \tag{13}$$

The governing equations in either spherical or Cartesian coordinates include derivative terms of the first order, but impart higher-order effects from the vertical velocity, bottom slope, and sea-surface gradient through the nonhydrostatic pressure. Except for the addition of the linearized vertical momentum equation and the nonhydrostatic pressure in the horizontal momentum equations, the system has the same structure as the nonlinear shallow-water equations.

Boussinesq Form and Linear Properties

There are parallels between the nonhydrostatic and Boussinesq-type approaches in spite of their distinct mathematical formulations. The nonhydrostatic pressure in the vertical momentum Eq. (12) can be expressed in terms of the horizontal velocity and sea surface elevation through the kinematic free surface and bottom boundary conditions. Substitution of this nonhydrostatic pressure into the horizontal momentum Eqs. (10) and (11) yields the Boussinesq form of the governing equations with vertical flow dynamics expressed as higher-order derivatives of the horizontal velocity. After dropping the nonlinear and tsunami excitation terms, the governing equations for flows in the x-direction read

$$\frac{\partial \zeta}{\partial t} + \frac{\partial (Uh)}{\partial x} = 0 \tag{14}$$

$$\frac{\partial U}{\partial t} + g\frac{\partial \zeta}{\partial x} - \frac{1}{4}h^2\frac{\partial^3 U}{\partial t \partial x^2} - \frac{3}{4}h\frac{\partial h}{\partial x}\frac{\partial^2 U}{\partial t \partial x} = 0 \tag{15}$$

which have the same form as the Boussinesq-type equations of Peregrine (1967), but with $1/4$ and $3/4$ instead of $1/3$ and 1 as the coefficients of the third-order dispersion and second-order bottom-slope terms. The variation of the coefficients leads to distinct dispersion and shoaling properties that illustrate a fundamental difference between the two approaches.

The dispersion relation is a primary performance indicator for depth-integrated wave models. Substitution of a linear periodic wave system in uniform depth with angular frequency ω and wave number k in Eqs. (14) and (15) yields the celerity for the nonhydrostatic approach that reads, along with its Taylor series expansion, as

$$c_{Nh} = \sqrt{gh}\left[1 + \frac{1}{4}(kh)^2\right]^{-1/2} = \sqrt{gh}\left[1 - \frac{1}{4}(kh)^2 + \frac{1}{16}(kh)^4 - \frac{1}{64}(kh)^6 + \frac{1}{256}(kh)^8 + o[(kh)^{10}]\right]^{1/2} \tag{16}$$

where $\sqrt{gh}$ is the shallow-water celerity; and kh is the depth parameter. The coefficient of ¼ from the governing equations is carried over to the leading-order $(kh)^2$ term in the dispersion relation resulting in non-monotonic convergence as $kh \to 0$, in contrast to Peregrine (1967) and Airy wave theory:

$$c_{Pg} = \sqrt{gh}\left[1 + \frac{1}{3}(kh)^2\right]^{-1/2} = \sqrt{gh}\left[1 - \frac{1}{3}(kh)^2 + \frac{1}{9}(kh)^4 - \frac{1}{27}(kh)^6 + \frac{1}{81}(kh)^8 + o[(kh)^{10}]\right]^{1/2} \tag{17}$$

$$c_{Airy} = \sqrt{gh}\left[\frac{\tan h(kh)}{kh}\right]^{1/2} = \sqrt{gh}\left[1 - \frac{1}{3}(kh)^2 + \frac{2}{15}(kh)^4 - \frac{17}{315}(kh)^6 + \frac{62}{2835}(kh)^8 + o[(kh)^{10}]\right]^{1/2} \tag{18}$$

Bai et al. (2018) showed this property is a result of the depth-averaged vertical velocity and nonhydrostatic pressure being computed from linear profiles. Full equivalence to the Boussinesq-type approach and asymptotic convergence of the dispersion relation can only be achieved with a quadratic distribution of the nonhydrostatic pressure (Jeschke et al. 2017).

The group velocity, which reduces to the shallow-water celerity as $kh \to 0$, describes the shoaling process through conservation of energy flux. Madsen and Sørensen (1992) introduced the linear shoaling gradient to evaluate model effectiveness in describing variation of wave amplitude $A(x)$ over a gentle slope as

$$\gamma = -\frac{h}{A}\frac{\partial A}{\partial x} \Big/ \frac{\partial h}{\partial x} \tag{19}$$

Substitution of a periodic system with variable wave number $k(x)$ into Eqs. (14) and (15) gives a relationship between $\partial A/\partial x$ and $\partial h/\partial x$ to derive the shoaling gradient for the nonhydrostatic approach as

$$\gamma_{Nh} = \frac{1}{4} - \frac{3}{16}(kh)^2 \tag{20}$$

For comparison, a parallel analysis of Peregrine (1967) and Airy wave theory gives

$$\gamma_{Pg} = \frac{1}{4} - \frac{1}{4}(kh)^2 - \left(\frac{\sqrt{3}}{9} - \frac{1}{6}\right)(kh)^4 \tag{21}$$

$$\gamma_{Airy} = \frac{1}{4} - \frac{1}{4}(kh)^2 + \frac{1}{18}(kh)^4 + \frac{1}{540}(kh)^6 - \frac{11}{3150}(kh)^8 + o[(kh)^{10}] \tag{22}$$

All three shoaling gradients converge to the maximum value of $1/4$ as $kh \to 0$, corresponding to the property of the shallow-water equations. The series truncation in Eqs. (20) and (21) indicates that both the one-layer nonhydrostatic approach and the Boussinesq-type equations of Peregrine (1967) are applicable to long waves such as tsunamis. The latter has an additional $(kh)^4$ term, but its opposite sign to that derived from Airy wave theory suggests a more rapid divergence with kh, as illustrated by Bai et al. (2018).

Numerical Procedures

The quasi three-dimensional system defined by Eqs. (4)–(8) already includes the numerical framework in the z direction through prescribed linear distributions of the vertical velocity and nonhydrostatic pressure. A staggered finite-difference scheme discretizes the computational domain in the (λ, ϕ) directions. The depth-averaged horizontal velocity components U and V are defined at the respective cell interfaces, while the surface elevation ζ, depth-averaged vertical velocity W, and nonhydrostatic pressure Q are defined at the cell centers. The computational grid differentiates wet and dry cells by the flow depth D and tracks any advancement of the wet-dry interface through extrapolation of (U, V) and ζ from the wet to dry cells (Kowalik and Murty 1993b). The spatial derivatives are computed by second-order central differences. Despite availability of higher-order methods (e.g., Harten 1983), the flux terms in the continuity equation is preferably computed by the first-order upwind scheme of Mader (2004). The resulting advective speed is implemented with the shock-capturing method of Stelling and Duinmeijer (2003) for modeling of discontinuous flows such as bores and hydraulic jumps. Mader (2004) extrapolates the surface elevation instead of the flow depth from the upwind cell and calculates the flux terms from the averaged water depth between two adjacent cells. This approach avoids errors from depth extrapolation and any discontinuity is due entirely to the surface elevation. The first-order upwind scheme is known to be dissipative, but helps stabilize the computation for energetic breaking waves and flux-dominated swash processes over irregular bathymetry and topography.

The fractional-step approach links the hydrostatic and nonhydrostatic components for a robust solution in time (e.g., Casulli and Stelling 1998). An explicit first-order integration of the horizontal momentum Eqs. (5) and (6), with the nonhydrostatic terms omitted, provides an initial estimate for the horizontal velocity $(\tilde{U}, \tilde{V})$ at the new time step $(t + \Delta t)$. The horizontal velocity (U, V) is then expressed in terms of the initial estimate $(\tilde{U}, \tilde{V})$ and the nonhydrostatic pressure Q. The vertical momentum Eq. (7) is integrated to give the vertical surface velocity w_s in terms of Q and the vertical bottom velocity w_b from the kinematic boundary condition in Eq. (3). The nonhydrostatic pressure is negligible in shallow-water flows and is set to be zero at the wet cells along the wet-dry interface for improved stability (Stelling and Zijlema 2003). Substitution of the U, V, and w_s into the conservation of mass defined by Eq. (8) yields a linear system of Poisson-type equations to determine Q at $(t + \Delta t)$. This in turn provides an update for (U, V) from integration of the nonhydrostatic terms in the horizontal momentum equations and an implicit integration of the continuity Eq. (4) for the surface elevation ζ before advancing to the next time step. Li and Cheung (2019) showed this semi-implicit first-order time integration from Kowalik and Murty (1993a) introduces second-order truncation properties identical to the commonly-used leapfrog scheme for the nonlinear shallow-water equations (Imamura et al. 1988).

The depth-integrated formulation cannot describe overturning of the free surface and thus does not fully reproduce breaking waves. The shock-capturing scheme approximates wave breaking as bore formation and imposes mass and momentum conversation across the flow discontinuity to account for energy dissipation without predefined mechanisms. These shock-related hydraulic processes are crucial for computation of wave runup at the shore (Wei et al. 2006), but present a challenge to the nonhydrostatic approach, in which the governing equations counteract flow discontinuities from the numerical scheme with frequency dispersion even in a flux-dominated regime. To circumvent this internal model confliction for long-wave computation, NEOWAVE deactivates the nonhydrostatic terms at computational cells when the flow speed reaches half of the shallow-water celerity:

$$\frac{\sqrt{U^2 + V^2}}{\sqrt{gD}} > 0.5 \tag{23}$$

The governing equations locally reduce to the nonlinear shallow-water equations for bore formation and energy dissipation, while the rest of the computational domain remains dispersive. The nonhydrostatic terms are reactivated when

$$\frac{\sqrt{U^2 + V^2}}{\sqrt{gD}} < 0.15 \tag{24}$$

The breaking initiation and cessation criteria, which were determined from numerical experiments for model stability, are consistent with laboratory observations from Sato and Kabiling (1994) and Okamoto and Basco (2006). Because the flow covered by these criteria is flux dominated, local deactivation of the nonhydrostatic terms avoids spurious oscillations across discontinuities without abruptly altering the overall flow conditions. This provides a practical approach to include flow discontinuities in nonhydrostatic modeling of tsunami waves (Yamazaki et al. 2012).

Grid nesting is essential for modeling of multiscale processes from transoceanic propagation to coastal inundation. Most grid-nesting schemes for tsunami modeling use the fluxes as input to a finer, inner grid and the surface elevation as feedback to the outer grid (e.g., Imamura et al. 1988; Liu et al. 1995). The present model inputs the horizontal velocity, surface elevation, and nonhydrostatic pressure to ensure propagation of breaking and dispersion waves across intergrid boundaries. These parameters from an outer grid are interpolated in time and space to provide the boundary conditions to an inner grid. The nonhydrostatic solution is implicit and requires reorganization of the Poisson-type equation system for the input non-hydrostatic pressure. The simple dispersion terms with first-order derivatives allow implementation of the Dirichlet condition at intergrid boundaries to ensure continuity of the

nonhydrostatic solution across multiple grid levels. After the computation in the inner grid reaches the outer grid time step, the surface elevation at the outer grid is updated with the average value from the overlapping inner grid cells to complete the procedure. The two-way intergrid data transfer is robust and accurate, with validated results for grid refinement ratios of up to 10 at the rugged Hawaii shore (e.g., Cheung et al. 2013; Lay et al. 2013; Bai et al. 2014, 2022; Li et al. 2016b). In addition, the grid-nesting scheme utilizes a flexible indexing system that enables adaptation of intergrid boundaries to topographic features for optimal resolution and computational efficiency, as demonstrated by Yamazaki et al. (2011a).

Numerical Dispersion

Finite-difference and time-integration schemes introduce truncation errors that interfere with the dispersion property of the governing equations (Abbott et al. 1984). Understanding such behaviors is important for model implementation and interpretation of computational results. Li and Cheung (2019) derived a dispersion relation using a linearized form of the governing Eqs. (9)–(12) for the discretization schemes in NEOWAVE. With uniform depth, the term $\partial w/\partial z$ in the conservation of mass defined by Eq. (13) is given by $2W/h$ for the linear vertical profile and the equation system is closed. Implementation of the staggered difference scheme and the semi-implicit time integration gives a system of algebraic equations for the five variables, ζ, U, V, W, and Q, in terms of the time step Δt and grid size $(\Delta x, \Delta y)$. Substitution of a linear periodic wave system with angular frequency ω and wave number $\vec{k} = (k_x, k_y)$ yields a homogeneous matrix equation. An eigenvalue of the determinant links the wave frequency and number in a dispersion relation for the discretized nonhydrostatic system with the celerity expressed as

$$c_{Nh,\Delta} = \sqrt{gh}\frac{1}{Cr(k\Delta x)}\arccos\left\{1 - \frac{2Cr^2(k\Delta x)^2[2-\cos(k_x\Delta x)-\cos(\sqrt{k^2-k_x^2}\Delta x)]}{2(k\Delta x)^2+(kh)^2[2-\cos(k_x\Delta x)-\cos(\sqrt{k^2-k_x^2}\Delta x)]}\right\} \tag{25}$$

where kh = depth parameter; $k\Delta x$ = spatial discretization parameter; and $Cr = \sqrt{gh}\Delta t/\Delta x$ is the Courant number with $\Delta x = \Delta y$ for illustration here.

The dispersion relation given by Eq. (25) is exact for the discretized governing equations, but does not reveal the interplay between the depth and discretization parameters. To illustrate the leading-order structure, we expand the cosine functions by Taylor series to show separately the intrinsic and numerical properties from the governing equations and discretization schemes as

$$c_{Nh,\Delta} = \sqrt{gh}\left\{\frac{1}{1+\frac{1}{4}(kh)^2} - \frac{\frac{1}{12}(k\Delta x)^2(\beta - Cr^2)}{\left[1+\frac{1}{4}(kh)^2\right]\left[1+\frac{1}{4}(kh)^2-\frac{\beta}{24}(kh)^2(k\Delta x)^2\right]} + o(\Delta x^4, \Delta t^4)\right\}^{1/2} \tag{26}$$

where $\beta = 1 - 2k_x^2k_y^2/k^4$ varies between 1 and 0.5 for waves propagating along the principal axes and the diagonal. The governing equations impart dispersion through the depth parameter kh in the first term, lowering the celerity from the shallow-water approximation. The spatial discretization $k\Delta x$ in the second term further reduces the celerity from numerical dispersion, while the Courant number Cr plays a secondary counteracting role because of its presence in the numerator only and its product with $k\Delta x$ resulting in a combined fourth-order term. Oblique wave propagation with $\beta < 1$ has lower numerical dispersion due to reduction in the effective grid spacing and Cr must be less than $1/\sqrt{2}$ for wave propagation over a two-dimensional grid. When $kh = 0$, the model becomes hydrostatic and gives the celerity as

$$c_{H,\Delta} = \sqrt{gh}\left[1 - \frac{1}{12}(k\Delta x)^2(\beta - Cr^2) + o(\Delta x^4, \Delta t^4)\right]^{1/2} \tag{27}$$

where the second term denotes the leading-order truncation errors from the discretization. For wave propagation along a principal axis with $\beta = 1$ and in the absence of $o(\Delta x^4, \Delta t^4)$, Eq. (27) becomes identical to the dispersion relation derived by Imamura et al. (1988) for the leapfrog scheme, which has the same truncation properties to second order.

A close look at Eq. (26) reveals that the intrinsic dispersion through kh in the first term is also present in the second term to decrease the effects of the leading-order truncation errors in comparison to the hydrostatic computation represented by Eq. (27). The dispersion relation (Eq. 26) of the numerical solution reduces to Eq. (16) from the governing equations as $k\Delta x \to 0$, indicating convergence of the discretization schemes. Li and Cheung (2019) conducted a series of numerical experiments to verify the convergence properties elucidated by Eqs. (26) and (27) for hydrostatic and nonhydrostatic modeling and to illustrate the limitations of using numerical dispersion directly from a shallow-water model to describe transoceanic propagation of tsunamis. Introducing $\Delta x^2 = \alpha h^2 + gh\Delta t^2$, which is a generalization from Imamura et al. (1988), gives

$$c_{Nh,\Delta} = \sqrt{gh}\left\{\frac{1+\left[\frac{1}{4}-\frac{\alpha(\beta-Cr^2)}{12(1-Cr^2)}\right](kh)^2 - \frac{\alpha\beta}{24(1-Cr^2)}(kh)^4}{1+\frac{1}{2}(kh)^2+\left[\frac{1}{16}-\frac{\alpha\beta}{24(1-Cr^2)}\right](kh)^4 - \frac{\alpha\beta}{96(1-Cr^2)}(kh)^6} + o(\Delta x^4, \Delta t^4)\right\}^{1/2} \tag{28}$$

The parameter $\alpha = (\Delta x^2 - gh\Delta t^2)/h^2$ combines the effects of grid size, time step, and water depth to indicate the level of numerical dispersion relative to the intrinsic property from the governing equations. A comparison between Eqs. (16) and (28) shows the discretization augments the dispersion relation from a [0, 2] to a [4, 6] rational function along with α for model optimization or error assessment.

We consider waves propagating along the x axis to illustrate the relationship between numerical and intrinsic dispersion. Because the time step plays a secondary role in numerical dispersion, we assign a small value of $Cr = 0.01$ to focus on the effects of spatial discretization. With $\Delta t \to 0$, the parameter $\alpha = (\Delta x/h)^2$ provides a measure of numerical versus intrinsic dispersion in modulating wave propagation

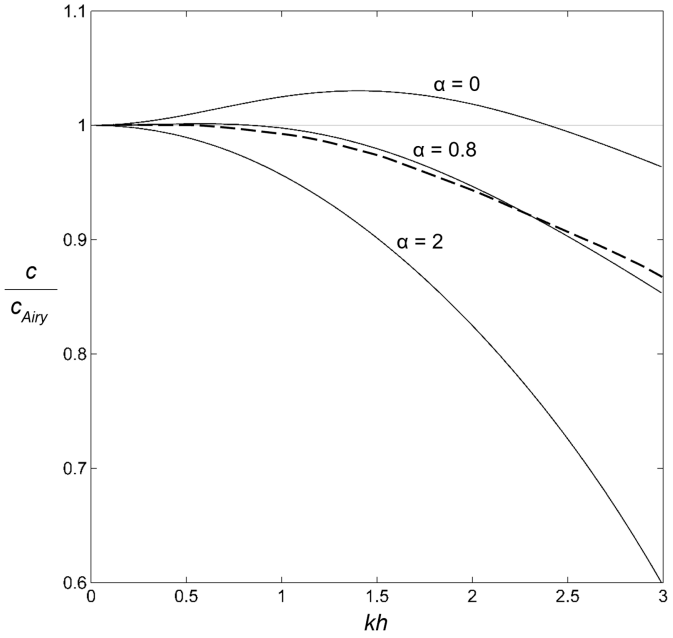

Fig. 2. Celerity for depth-integrated free-surface flow normalized by the exact solution from Airy wave theory versus water depth parameter kh. Dashed and solid lines denote dispersion relations from the Boussinesq-type equations of Peregrine (1967) and the nonhydrostatic approach for a plausible range of α with $\Delta t \to 0$.

across the computational grid. Fig. 2 compares the celerity from the Boussinesq-type equations of Peregrine (1967) in Eq. (17) and the dispersion relations defined by Eqs. (16) and (25) for the governing equations and their discretized form in the nonhydrostatic approach. The results are normalized by the exact solution from Airy wave theory in Eq. (18) to provide the percentage error as a function of the depth parameter. The Boussinesq-type equations perform very well in the typical tsunami range of $kh = 0$–0.6 due to its asymptotic convergence behavior. For $\alpha = 0$ in the absence of numerical effects, the governing equations show weaker dispersion properties and overestimate the celerity for $kh < 2.4$ due to an assumed linear profile of the nonhydrostatic pressure. Increasing α introduces numerical dispersion and reduces the celerity. A value of $\alpha = 0.8$ produces the right amount of numerical dispersion to offset the underestimation from the governing equations and reproduces the celerity up to $kh = 0.6$ and 1.2 with less than 0.13% and 0.77% error relative to Airy wave theory. The resulting dispersion relation follows closely the Boussineq-type equations of Peregrine (1967) for modeling of frequency dispersion and has slightly better performance over most of the intermediate depth range, which covers short-period superharmonics generated by nonlinear tsunami processes over seamounts and in coastal waters (Bai and Cheung 2016). Further increase of the cell size relative to the water depth will introduce excess numerical dispersion in the model results.

Model Benchmarking

NEOWAVE is a community model with a track record for seismological and tsunami research, coastal and maritime hazard assessment, and infrastructure planning and design (e.g., Bletery et al. 2014; Yim et al. 2014; Catalán et al. 2015; Yamazaki et al. 2018; Wood et al. 2019; Salazar et al. 2022). Such applications require an accurate description of tsunami generation, dispersion, shoaling, bore formation, and currents. While the preceding section evaluated the fundamental properties of dispersion and shoaling against approximate and exact solutions, the remaining processes with different spatial and temporal scales can be isolated in numerical and laboratory experiments to serve as proxies for tsunami model benchmarking.

Tsunami Generation

A key feature of the nonhydrostatic approach is the capability to model tsunami generation from time histories of seafloor deformation. The excitation is transmitted from the vertical momentum equation to the horizontal momentum equations through the nonhydrostatic pressure. The process accounts for spreading and attenuation of the seafloor excitation to the sea surface versus the use of the final seafloor displacement as a static initial sea-surface pulse in the hydrostatic and Boussinesq-type approaches. The limitation of the static initial condition was recognized by Kajiura (1963), who proposed a filter based on Green's theorem to account for transmission of the seafloor displacement through the water column. The nonhydrostatic approach can include a rise time to describe the initial fluid motion dynamically, but is subject to the predefined vertical flow structure in the governing equations. Through a numerical experiment, we utilized the Navier-Stokes model of Horrillo (2006), based on the volume of fluid method without predefined vertical flow structures, as a benchmark to evaluate the present depth-integrated approach in describing tsunami generation. The computational domain is 400 km long, 50 km wide, and 5 km deep with a frictionless bottom. The discretization involves a cell size of $\Delta x = \Delta y = 500$ m and a Courant number of $Cr = 0.22$, which is within the range commonly used for practical application of NEOWAVE. The staggered finite-difference grid includes 80,901 cell-center and 80,000 cell-interface nodes for time integration of the surface elevation and horizontal velocity, respectively, while the one-layer parameterization leads to a Poisson-type equation for the nonhydrostatic pressure at the cell-center nodes.

The vertical seafloor displacement is defined by a Gaussian hump rising linearly to a height of $a = 5$ m over 10 s along the length of the computational domain. The wave generation processes are primarily linear and the model results are presented in dimensionless form for direct comparison. Fig. 3 plots the computed sea surface elevations and the input vertical seafloor displacement over a patch denoted by effective width b. Because the resulting wave period is much longer than the rise time τ of 10 s, wave propagation is negligible during the seafloor uplift. The height of the initial wave increases by a factor of two from $\tau/2$ to τ. The generation processes are primarily hydrostatic for a wide seafloor deformation patch with $b/h = 40$. The computed sea surface elevations from NEOWAVE and the Navier-Stokes model are very close to the input seafloor vertical displacement. As b/h decreases, the computed initial wave becomes lower and more spread out compared to the seafloor displacement due to transfer of momentum from the vertical to horizontal directions. NEOWAVE tends to overestimate the vertical momentum transfer and underestimate the horizontal energy spreading due to the limited degree of freedom in the prescribed vertical flow structure. The computed initial wave is 10% higher than the Navier-Stokes model for $b/h = 4$, in which the resulting waves are well into the intermediate depth range. The use of the final seafloor displacement as the static initial condition will lead to overestimation of the wave height by 67%. With the same displaced volume, the reduced footprint will lead to shorter-period waves further distorting the tsunami waveform. The information provides useful guidance for tsunami

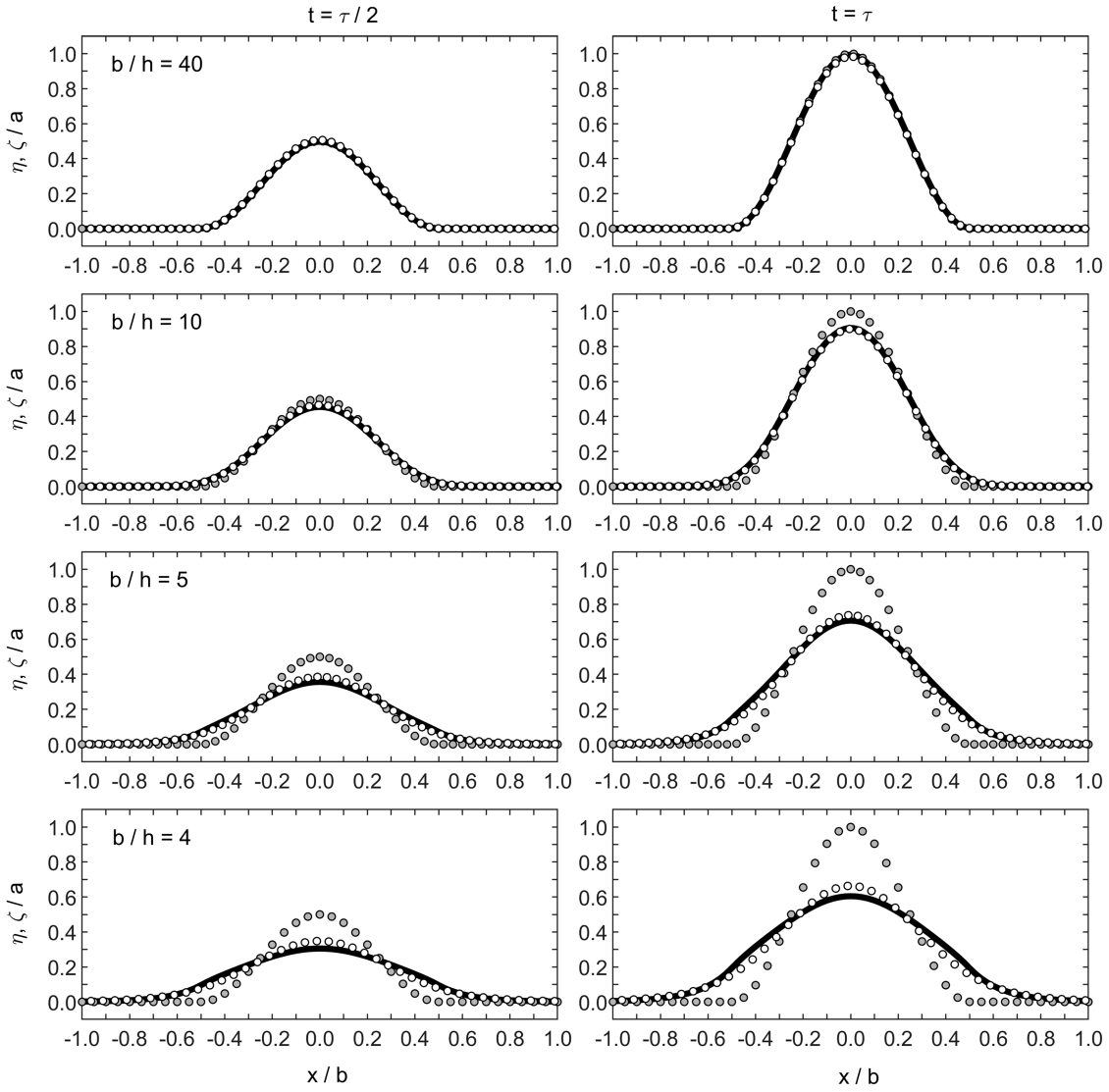

Fig. 3. Seafloor displacement (grey circle) defined by a Gaussian hump and computed sea-surface elevations from NEOWAVE (white circles) and the Navier-Stokes model (black line) of Horrillo (2006) over a rise time of $\tau = 10$ s.

modeling with detailed seafloor deformation obtained from finite-fault models of earthquake rupture.

Bore Formation

The National Science Foundation (NSF) sponsored an inundation model workshop at Oregon State University in 2009. The workshop utilized two laboratory experiments performed in a wave basin 48.8 m long and 26.5 m wide to provide a blind test for 10 numerical models developed in the US and Europe. Lynett et al. (2019) provided a detailed description of the experiments and the full array of data collected. Fig. 4 shows the relief model and instrumentation arrangement for the more challenging second experiment referred as Benchmark II at the workshop. The water depth was 0.78 m at the wave maker in its neutral position. The main relief features included a triangular reef flat submerged between 7.5 and 9 cm below the still-water level and a cone of 6 m diameter and 0.45 m height fitted to the apex. The reef sat on a segmented background profile with lower and upper slopes of 1:16 and 1:32. The steep 1:3.5 slope at the reef apex flared to 1:16 over a distance of 9 m on either side with abrupt transitions to the background profile. The top of the relief model varied from 0.16 to 0.13 m above the still-water level toward the back wall. The surface was uneven due to artifacts of the physical model construction, but was well resolved by a laser scan for input to numerical models. The incident solitary wave had a height of $H = 0.39$ m giving rise to strongly nonlinear conditions with $H/h = 0.5$. The resulting flow conditions were recorded by wave gauges, acoustic Doppler velocimeters, and three video cameras mounted above the basin to provide a benchmark for model assessment.

The computational domain was set up in Cartesian coordinates with x normal to the wave maker, a cell size of $\Delta x = \Delta y = 0.05$ m, a Courant number of $Cr = 0.04$, and a Manning's number of $n = 0.012$ for subgrid roughness of the finished cement surface. The spatial discretization involved 461,100 cell-center and 462,501 cell-interface nodes with the laser-scanned relief model defined at the former without any smoothing. Fig. 4 provides a series of surface elevation snapshots as the solitary wave transforms over the reef and slope complex. In the laboratory experiment, spilling at the crest occurred locally, when the solitary wave reached the reef apex at $t = 6$ s. With rapid shoaling over the steep reef slopes, a plunging breaker developed across the triangular reef and overtopped the

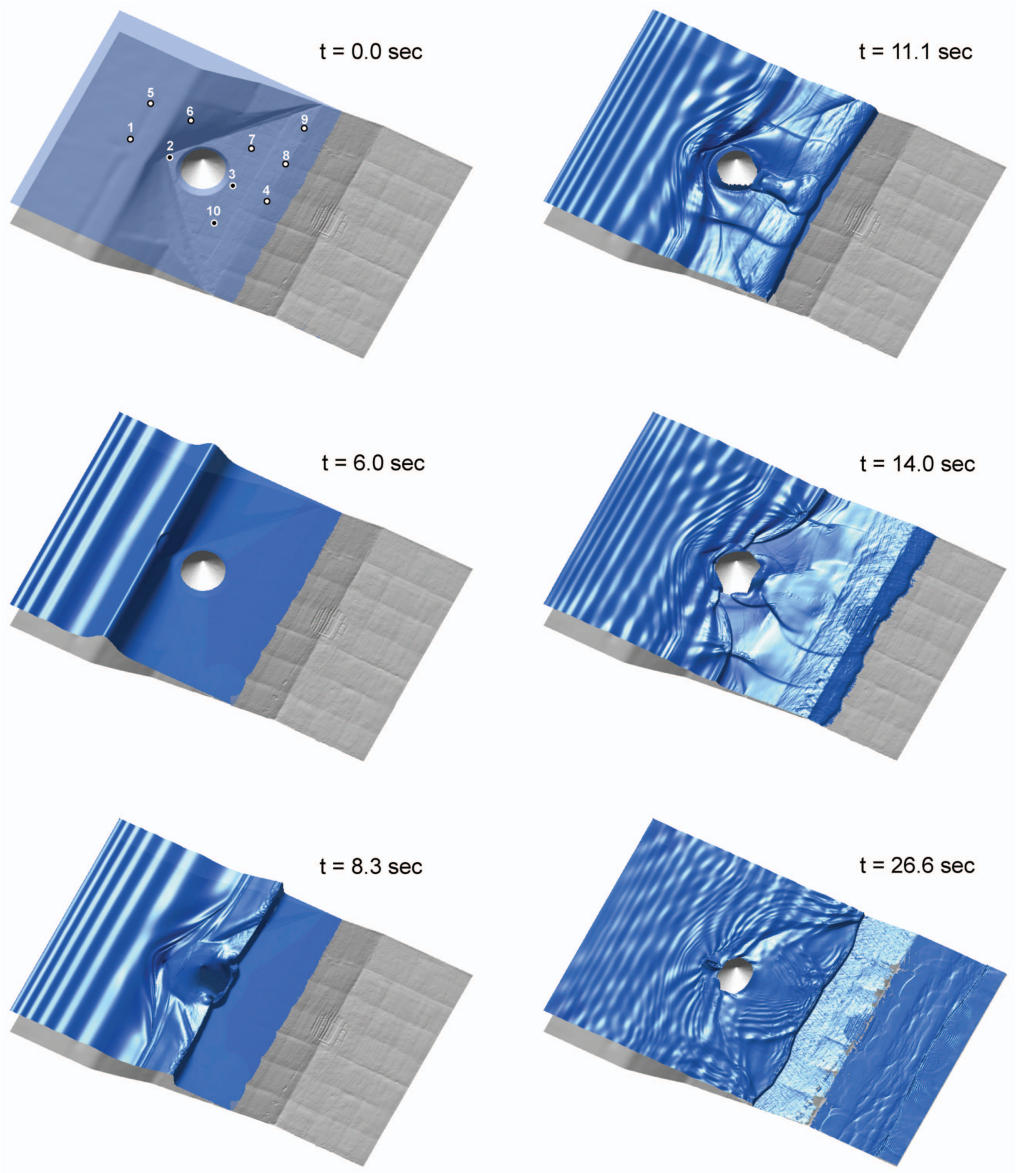

Fig. 4. (Color) Relief model, instrument locations, and computed surface elevation sequence for Benchmark II of the 2009 NSF inundation model workshop at Oregon State University. Circles in the panel $t = 0.0$ s denote wave gauge locations and those with darkened core indicate collocation with acoustic Doppler velocimeters.

entire cone at $t = 8.3$ s. The model approximates the initial spilling as a local discontinuity at the crest and the subsequent plunger as a collapsing bore with flow discontinuities spreading across several cells. The refracted waves from the reef slopes and the diffracted waves around the cone converge in the back, when the bore reached the initial waterline at $t = 11.1$ s. The bore collapsed into a surge moving up the initially dry slope and reaching the top by $t = 14.0$ s. The reflection from the wave maker arrived at the reef edge, while the refracted and diffracted waves from the initial arrival were wrapping around cone. At $t = 26.6$ s, the receding sheet flow generated a hydraulic jump near the initial waterline that coincide with an incoming bore from the wave-maker reflection. As observed in the laboratory experiment, the upper slope began to dry with water trickling down the irregular cement surface. The sheet flow on the top continued to move forward in the presence of a reflected bore due to water backing up from the end wall.

The recorded datasets from the laboratory experiment allow qualitative and quantitative comparisons with the numerical model results. As shown in Fig. 5, the video images compare very well with the aforementioned bores and hydraulic jumps as well as the complex wave processes around the cone. The depth-integrated model is able to capture the most violent flow from plunging of the solitary wave on the cone. The down rush from the overtopping generates a hydraulic jump on the leeside that in turn feeds a bore propagating toward the initial waterline. The computed velocity and vorticity at $t = 8.3$ s suggest generation of strong rotational flows at the confluence of the down rush from the cone and the impulsive flow from breaking of the refracted wave over the adjacent reef slope on either side. Dye released at the location during the experiment shows trajectories that are well corroborated by the sequence of computed vorticity fields. Both suggest migration of a vortex pair from the cone to near the initial waterline during the incoming flow and generation of a second vortex pair by interactions of the receding flow with the wave-maker reflection and the trapped waves around the cone at $t = 26.6$ s. In addition to vortex formation, this benchmark presents a number of challenges to

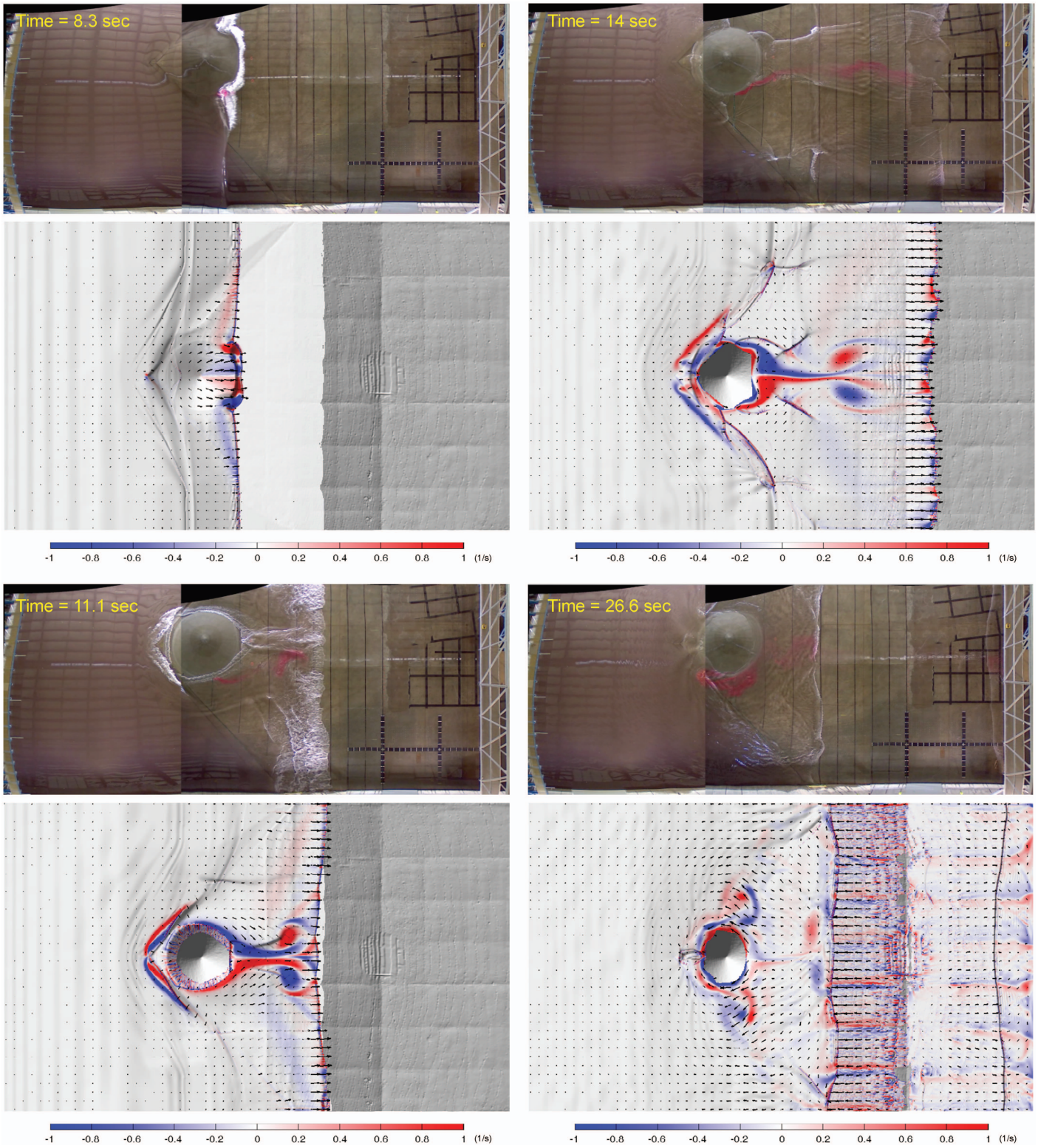

Fig. 5. (Color) Comparison of video recorded wave and dye transport patterns with computed surface elevation (light grey shading), flow velocity (vector), and vorticity (red and blue tone for clockwise and counterclockwise rotations) for Benchmark II of the 2009 NSF inundation model workshop at Oregon State University.

numerical models. The bores during the incoming flow are highly turbulent, as inferred from the trailing air entrainment in the video images at 8.3 and 11.1 s. The receding sheet flow on the upper slope is gradual, but as illustrated in the numerical model output at 26.6 s, involves localized, rapid drying over the uneven surface as well as its top edge, which transitions to a mild negative grade toward the back wall. The model stability for such rapidly varying and complex flows is beyond what can be gauged from the shallow-water celerity, providing an explanation for the very small Courant number of 0.04 used in the computation.

Fig. 6(a) compares the numerical model results with the recorded surface elevations during the experiment. Along the centerline, the model reproduces the incident solitary wave at Gauge 1 and its initial steepening at Gauge 2 across the steep reef slope, the video-observed turbulent bore at Gauge 3 from overtopping of the cone, and the bore driven by the subsequent down rush behind the cone at Gauge 4. These are followed by trapped waves around the cone, receding flow from the upper slope, and reflection from the wave maker. The results at Gauges 5 to 9, off the centerline, show similar wave patterns, but with reduced amplitudes of the trapped waves due to their distance from the cone. The agreement is generally good except at locations with turbulent bores, in which the extensive splashing and air entrainment might have interfered with instrument operation and influenced the propagation speed with cumulated effects over time. Fig. 6(b) shows good agreement of the x component of the velocity despite spilling of the wave crest over the reef apex at Gauge 2. The recorded data immediately behind the cone at Gauge 3 missed most of the breaking wave generated by the overtopping due to splashing and air entrainment. Both gauges were located along the centerline and the small recorded y component from the initial arrivals might be instrumentation artifacts or vortical flows not reproduced by the model. Gauge 10 on the side recorded the initial bore, showing good agreement with the computed velocity. The y component is a fraction of the x component, with distinct secondary flow features of which the overall trend is well accounted for. The qualitative and quantitative comparisons in this laboratory benchmark demonstrate the capability of the shock-capturing scheme in providing a first-order approximation to the complex hydraulic processes involving turbulent bores and hydraulic jumps commonly seen in destructive tsunami events.

Separation-Driven Currents

The National Tsunami Hazard Mitigation Program (NTHMP) organized a model benchmarking workshop on tsunami currents in 2015 (Lynett et al. 2017). The flume experiment of Lloyd and Stansby (1997) constituted Benchmark I for evaluation of 13 numerical models used in tsunami hazard assessments worldwide. Fig. 7(a) shows a schematic of the experiment involving a frustum 4.9 cm high submerged in a flume 5.4 cm deep. The frustum has top and bottom diameters of 5 and 75 cm with a gentle slope of 8.9°. The steady incoming current of 15.5 cm/s develops a wake with periodic vortex shedding behind the frustum. A particle tracking velocimetry (PTV) system recorded time series of the surface velocity at two locations in the wake. We set up a computational domain with 1, 2, and 4 cm grid spacing for a sensitivity analysis and an investigation of the numerical dissipation mechanism in relation to the physical processes. The modeled flume of 976 cm long and 152 cm wide leads to 149,481, 37,653, and 9,555 computational cells arranged symmetrically about the centerline. The total number of cell-center and interface nodes used in the computation is about two times the number of cells, depending on the grid configuration and boundary conditions. The initial series of tests used the same Courant number of 0.1 for the three grids to provide a reference. The Manning's number of $n = 0.01$ accounts for surface roughness of the flume and frustum, as suggested by Lloyd and Stansby (1997). The current was ramped up gradually to 15.5 cm/s at the upstream boundary and an open boundary condition was implemented at the downstream end to allow exit of the flow. The frustum remained submerged at all times during the laboratory and numerical experiments for a direct comparison of the results.

The results from the 2-cm grid spacing that are presented in Fig. 7(b) give the best match to the laboratory observations. The incoming uniform current deflects around the frustum creating a pair of symmetric vortices in the wake that gradually extend downstream and transform into a vortex street, as reported by Lloyd and Stansby (1997). Fig. 8 compares the computed and recorded velocity at the two PTV locations after steady-state flow conditions are developed. The flow includes a steady stream-wise component associated with the incoming uniform current and a periodic component in both directions due to vortex shedding. The recorded velocity also exhibits some unsteadiness associated with vertical mixing behind the apex of the frustum. The stream-wise velocity U immediately downstream at Location 1 is affected the most. The NEOWAVE results, which are based on depth-integrated governing equations, are not amenable to the three-dimensional turbulent flow in the wake. The depth-averaged current reproduces the short-period oscillations in the surface measurements but not the amplitude or the mean flow. The agreement is much better for the span-wise velocity V dominated by vortex shedding. The effects of vertical mixing abate at Location 2 off the centerline, where the computed time series demonstrate good agreement with the measurements in terms of amplitude, period, and phase for both U and V. The comparison at the two locations indicates a depth-integrated model can reproduce the eddy strength and shedding frequency as well as the primary structure of a vortex street through numerical means.

Numerical dissipation from the first-order upwind approximation is proportional to Δx^2 and Δt^{-1} in a nonlinear shallow-water model (Casulli 1990). The truncation errors might be modulated, but likely have similar effects in the nonhydrostatic computation. The process manifests as numerical viscosity in the otherwise inviscid flow that is traditionally regarded as an undesirable artifact and is a primary motivation for implementation of high-order schemes (e.g., Drikakis and Smolarkiewicz 2001), but becomes an ad hoc mechanism for generation of recirculating flow under high shear stress in long-wave models. The sensitivity analysis shows that an increase in the cell size, while maintaining the same Courant number, leads to growth in the amplitude and reduction in the period of the oscillatory flow. The computation remains stable for the range of cell sizes considered and produces steady-state oscillatory flows for many cycles. Additional tests show the Courant number has relatively minor effect on numerical dissipation as long as the CFL condition is satisfied. Varying the Manning's number from 0 to 0.01 shows little effect on the model results, signifying the dominance of numerical means in the generation and shedding of vortices under steady-state flow conditions. The cell size provides the primary mechanism for tuning of the eddy strength and frequency in practical application, but is to no avail in the absence of site-specific measurements a priori. Additional field benchmarks examined at the workshop suggest an optimal grid resolution of ~10 m for depth-integrated modeling of tsunami-induced currents in harbors (Lynett et al. 2017), corroborating earlier experiences with hydrostatic and nonhydrostatic modeling for Hawaii and Oregon coasts (e.g., Cheung et al. 2011, 2013).

Case Study

The 2011 Tohoku earthquake ruptured the subduction zone off northeastern Honshu with strong regional shaking and a destructive tsunami across the Pacific Ocean. The recorded geophysical and hydrographic datasets have facilitated development of earthquake and tsunami source models to explore the mechanisms and impacts of the event (Lay 2018). In particular, the source model

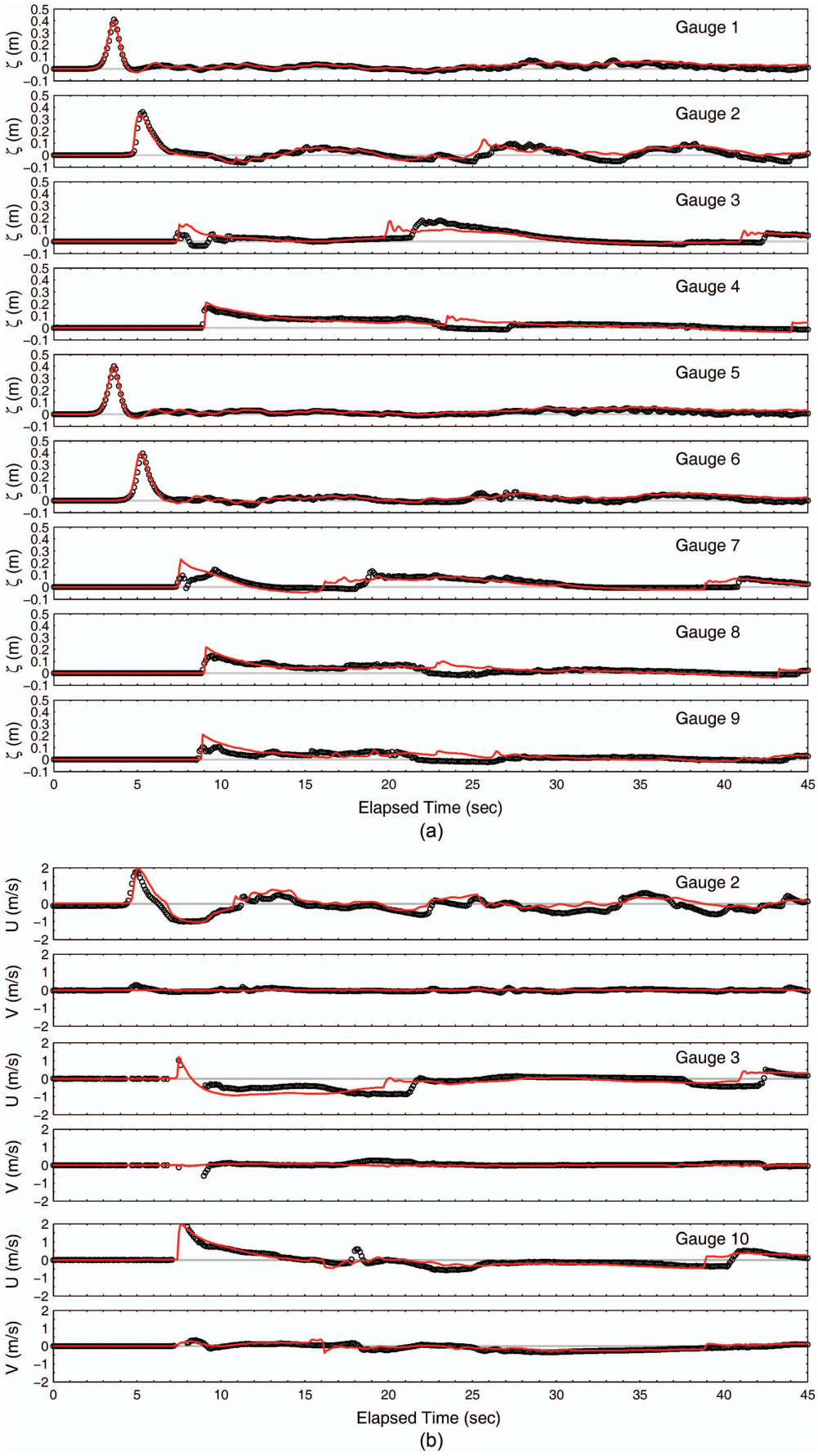

Fig. 6. (Color) Comparison of laboratory measurements (circles) and model predictions (red lines) for Benchmark II of the 2009 NSF inundation model workshop at Oregon State University: (a) Surface elevation; and (b) current velocity components. See Fig. 4 for instrument locations.

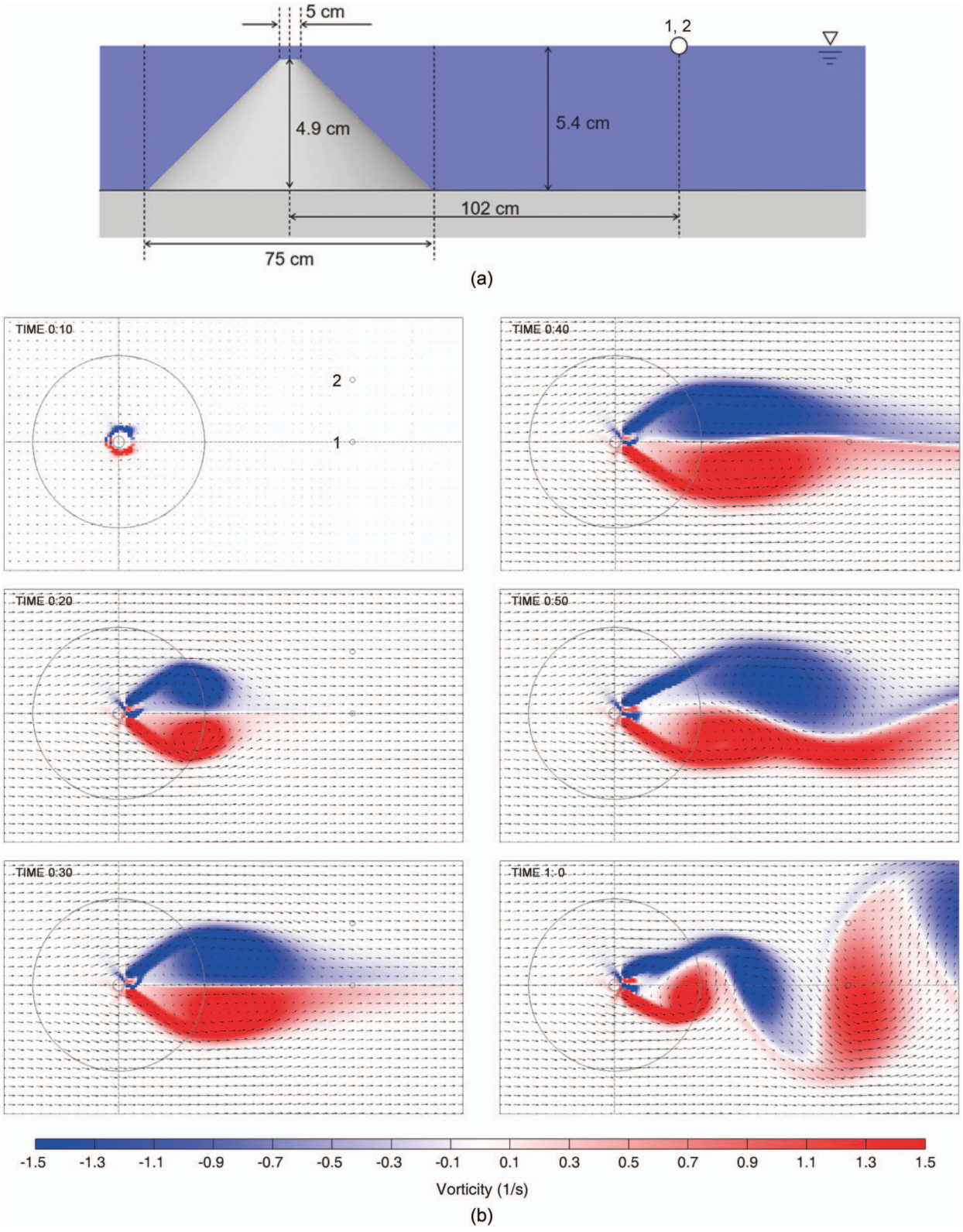

Fig. 7. (Color) Benchmark I of the 2015 NTHMP tsunami current workshop: (a) model setup in elevation view; and (b) computed flow velocity (vector) and vorticity (red and blue tone for clockwise and counterclockwise rotations). Large and small concentric circles delineate the frustum footprint and crest. Small circles with Labels 1 and 2 denote locations of particle tracking velocimeters.

of Yamazaki et al. (2018) consistently reproduces the global seismic and regional geodetic records as well as wave runup along 2,000 km of east Japan coasts, near-field waveforms at 18 buoys surrounding the tsunami source, and far-field records from 26 DART station across the north and south Pacific with NEOWAVE [see Figs. 9(a and b) for buoy and station locations]. In this case study, we reexamine the tsunami event with additional model results, observations, and insights from the benchmarks to highlight the enhanced capabilities achievable by the nonhydrostatic approach.

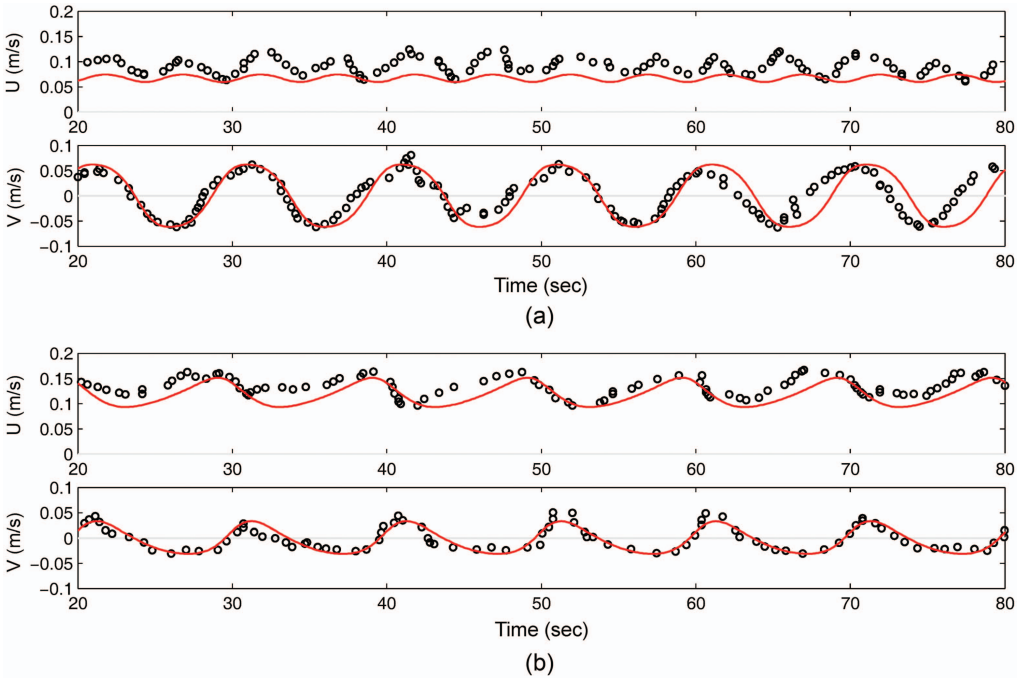

Fig. 8. (Color) Recorded (circles) and computed (red line) velocity components for Benchmark I of the 2015 NTHMP tsunami current workshop: (a) location 1; and (b) location 2, as shown in Fig. 7. Computed velocity is depth averaged, while recorded currents are at the water surface.

Model Setup

The case study utilizes up to four levels of two-way nested computational grids to describe multiscale tsunami processes. Fig. 9 shows the grid systems to illustrate the model regions. The Level 1 grids in Fig. 9(a) describe wave propagation over large-scale seafloor features across the ocean. The 2 arcmin (~3,600 m near Equator) resolution and the average ~4,000 m depth of the Pacific Ocean give optimal model dispersion properties (Fig. 2). The Level 2 grids in Figs. 9(b and c) describe wave transformation and resonance over continental margins or along island chains at 24 arcsec (720 m). The Level 3 grids in Fig. 9(d) cover large coastal features such as embayments, headlands or islands at 3 arcsec (90 m) and serve as a transition to the Level 4 grids in Fig. 9(e) with a target resolution of 0.3 arcsec (~9 m), which is optimal for harbor or coastal areas with breakwaters, channels, dunes, and tropical reefs (Cheung et al. 2011, 2013; Lynett et al. 2017). A Manning's number of $n = 0.025$ describes subgrid roughness of the seafloor. The Level 1, 2, 3, and 4 grids have varying size and resolution with computational cells in the range of 2,085,496–25,152,541, 518,941–2,363,821, 485,233–1,038,841, and 180,861–984,841, respectively. The two-way grid nesting becomes essential to provide high-resolution description near the entrance and instrument locations within the interconnected lagoon system at Humboldt Bay [Fig. 9(e)]. The digital elevation model includes GEBCO for the Pacific Basin as well as regional datasets available from the Japan Hydrographic Association, NOAA National Centers for Environmental Information, US Army Corps of Engineers, and Pacific Islands Benthic Habitat Mapping Center at the University of Hawaii. The source data resolution is as fine as 1 m, revealing the highly complex reef bathymetry at Honolulu and Apra Harbors even after being down-sampled to 9 m for tsunami modeling.

The finite-fault model of Yamazaki et al. (2018) defines the seafloor excitation as forcing to the boundary-value problem. The ruptured plate interface has a projected area of 240 km by 400 km and variable dip from 9° to 19°, based on the US Geological Survey Slab 1.0 model (Hayes et al. 2012). The slip distribution is described by a 6×10 grid of subfaults with 40×40 km^2 area and up to 32 s displacement rise time each. The rupture starts at the hypocenter (38.107°N, 142.916°E) 16.2 km beneath the continental slope and propagates radially out on the plate interface for 2.5 min. Fig. 10 shows the slip distribution, seafloor excitation, and sea-surface elevation at 1, 1.5, and 2.5 min after the earthquake origin time. The seafloor excitation, which includes 17.5% displacement volume from horizontal motion of the continental slope, shows expansion of subsidence toward the Tohoku coast and uplift in the offshore direction. Distinct regions of uplift develop near the epicenter and along the trench with significant influence on the resulting tsunami. The nonhydrostatic modeling is important to resolve the vertical flow generated by the large near-trench uplift as well as the inertia of the upswing from the initial sea-surface dropdown along the coast. The seafloor excitation spreads horizontally in the water column, producing a smoother pulse with reduced amplitude, while propagating away from the source simultaneously as surface waves. This results in distinct seafloor deformation and surface-wave patterns at the end of the rupture. The use of the final seafloor deformation as the initial sea-surface condition does not fully reproduce the near-field tsunami even with a nonhydrostatic model (Li et al. 2016a).

Waveforms and Currents

Nonhydrostatic processes continue to play an important role as the tsunami propagates away from the source. The complex wave system is illustrated by snapshots of the computed sea-surface elevation in Fig. 11 as well as a comparison of computed and recorded signals at selected offshore water-level stations in Fig. 12. The snapshots at 10 and 22 min after the earthquake origin time show three dominant wave components generated by the uplift in the near field. The initial pulse near the epicenter propagates outward as radial waves with a 60 min period, while the more impulsive

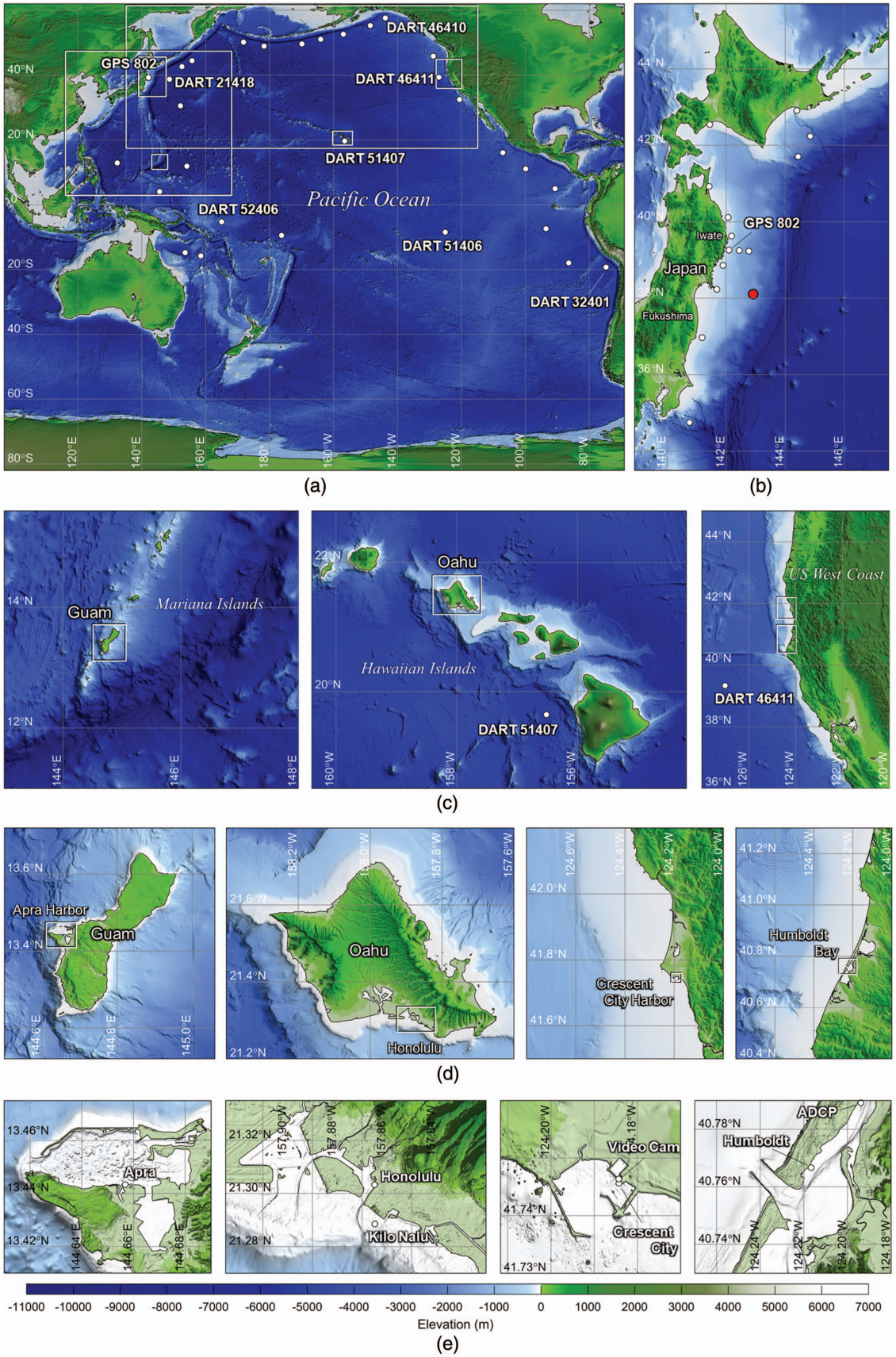

Fig. 9. (Color) Location maps and computational grids for modeling of the 2011 Tohoku tsunami: (a) Level-1 grid for Pacific-wide modeling and outlines of telescopic Level-1 and 2 grids for regional modeling; (b) Level-2 grid in the near field (red circle denotes the earthquake epicenter); (c) Level-2 grids in the far field with outlines of Level-3 grids; (d) Level-3 grids with outlines of Level-4 grids; and (e) Level-4 grids. White circles denote instrument locations and those with labels are considered in this paper. (DEM datasets from GEBCO, Japan Hydrographic Association, NOAA, US Army Corps of Engineers, and University of Hawaii—Pacific Islands Benthic Habitat Mapping Center.)

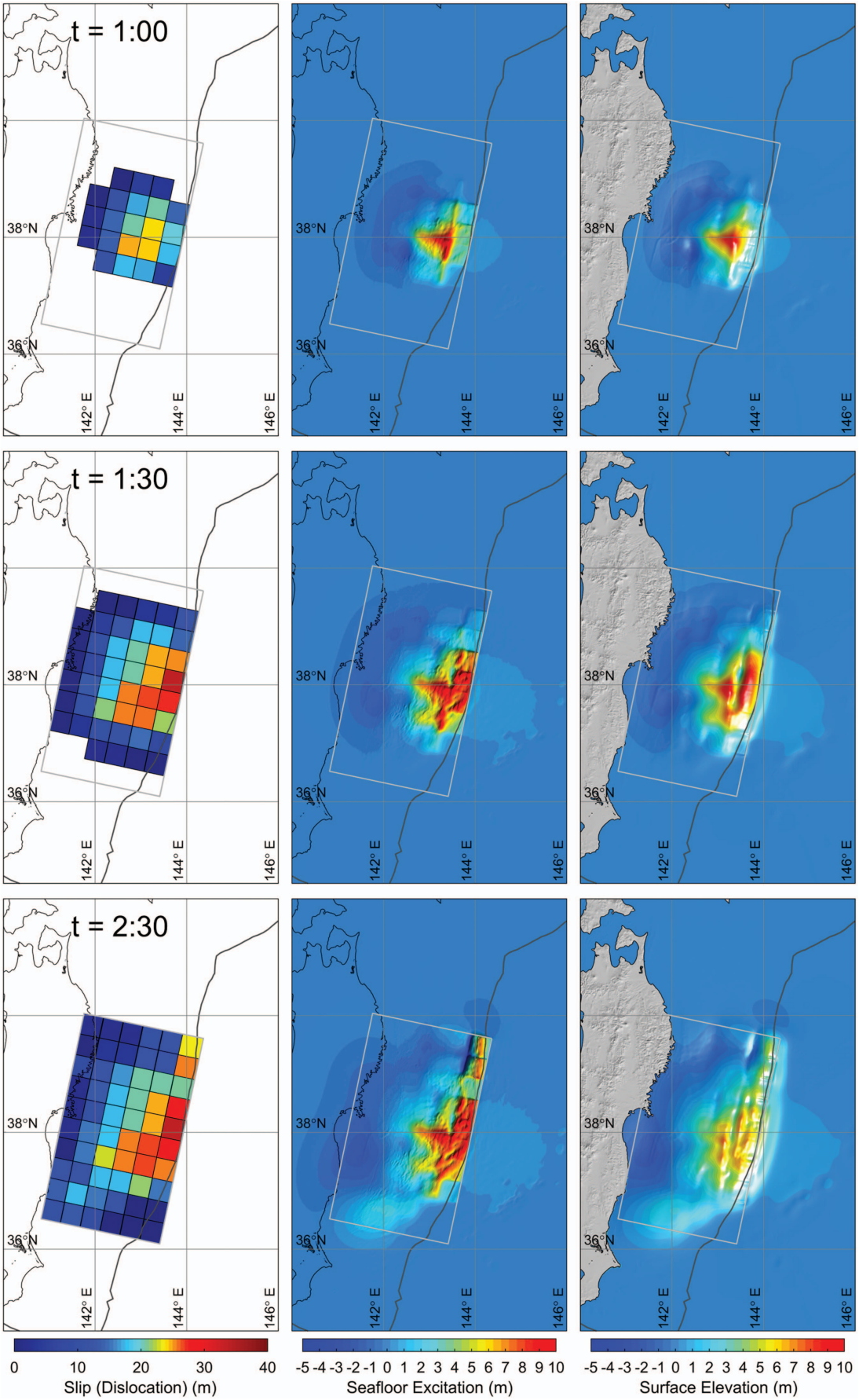

Fig. 10. (Color) Time histories of fault slip, seafloor excitation, and sea-surface elevation computed for the 2011 Tohoku earthquake and tsunami over the rupture duration of 2.5 min. Grey line denotes Japan Trench. (Background map from GEBCO's gridded dataset.)

excitation along the trench generated long-crested waves with a 45 min period. Diffraction of the long-crested waves to the north and south produces a 90-min component with smaller amplitude. These wave components and their interference produced distinct signals at nearshore buoys and varying impacts along east Japan coasts (Yamazaki et al. 2013, 2018). The two near-field snapshots show alignment of the initial radial and long-crested waves as they propagate toward the Iwate and Fukushima coasts at the northern and southern parts of the source region. The seafloor slope, which is part of the nonhydrostatic terms in the governing equations, deflects the incoming flow upward to alter the long-wave dynamics over the continental margin. Part of the quasi three-dimensional processes manifest as local dispersion modulating the propagation speed and phase of the incident waves despite reduced frequency dispersion in the onshore propagation over shoaling waters.

The superposed radial and long-crested waves reach GPS 802 off south Iwate at $t = 22$ min amidst the upswing from the initial sea-surface dropdown. The constructive interference results in recorded tsunami amplitude of 6.31 m over the shallow shelf and large runup of ~40 m on the rugged Sanriku coast (Mori et al. 2011). DART 21418 immediately offshore registers a large leading wave of 1.75 m amplitude from the long-crested component. Short-period trailing waves are evident at both locations despite their proximity to the source. The distinct leading wave is maintained albeit with considerable steepness reduction due to frequency dispersion along the southern and northern side lobes reaching DART 52406 near Solomon Islands and DARTs 46410 and 46411 off Alaska and California. As shown in the snapshot at $t = 8$ h, the many seamounts and atolls in the western and central Pacific produce prominent scattering of the tsunami waves with generation of short-period superharmonics, which are evident at DART 51407 near Hawaii. Superposition of the scattered and dispersed waves creates a diamond pattern with localized peaks and troughs behind the wave front. As the tsunami reaches the south Pacific, the trailing waves become more energetic and dominant, as seen in the h-16 snapshot and the signals at DART 51406 and 32401 toward north Chile.

The tsunami waves reaching the shore can be strongly influenced by local resonance with characteristics distinct from those in the open ocean. Fig. 13(a) compares the computed and recorded signals at selected tide gauges around the Pacific Ocean. The model results match the Honolulu tide gauge signals reasonably well, indicating reproduction of the wide range of incident wave components as well as the multiscale resonance from the harbor basin to the reef and shelf complex along the Hawaiian Islands (Cheung et al. 2013). The dominant 43-min component, which is also seen at DART 51407 (Fig. 12), is in the range of the long-crested waves generated by the large near-trench uplift. The good agreement is maintained across the ocean at Crescent City Harbor and Humboldt Bay, California, as well as Apra Harbor, Guam, where the tide gauges are located in embayments well sheltered by breakwaters or barrier islands from the open ocean [Fig. 9(e)]. Shelf resonance is also evident along the California coast, as indicated by the increasing wave amplitude after the initial arrivals at Crescent City Harbor and Humboldt Bay in spite of the large leading wave recorded at DART 46411 immediately offshore (Fig. 12). In the absence of an insular shelf around Guam, the tsunami waves in the well-sheltered Apra Harbor resemble those at nearby DART stations (Yamazaki et al. 2018). The embayment itself experienced persistent long-period oscillations between the outer and inner basins, with observed strong currents at the channel in between [Fig. 9(e)].

Coastal currents, which can be driven by multiple mechanisms, are more complex than sea-surface motion during a tsunami. Fig. 13(b) shows good agreement of the computed and recorded surface elevations and velocity components at Kilo Nalu Coastal Observatory, which operates a bottom pressure sensor and an ADCP atop a fringing reef at 12.2 m water depth and 400 m off the Honolulu shore [Fig. 9(e)]. The waves between 5 and 16 min periods have comparable or greater contributions to the currents, but much weaker surface signals compared to the dominant 43-min component. This is likely due to standing edge waves with distinct nodes and antinodes or separation-driven currents with much weaker surface signature over the fringing reefs. Fig. 13(c) provides a comparison of the current velocity in Crescent City Harbor and Humboldt Bay. Admire et al. (2014) inferred the current at the inner basin entrance of Crescent City Harbor from debris movement recorded by a video camera [Fig. 9(e)]. The inferred surface current along the entrance channel shows general correspondence of the phase and the 20–30 min dominant periods with the depth-averaged velocity from the numerical model. Both show jagged time series with short-period signals not present at the adjacent tide gauge, likely due to separation-driven flows from the harbor breakwater and basin entrance. Better agreement is obtained with the ADCP measurement in Humboldt Bay. The adjacent tide gauge signals have strong correlation with the current, indicating wave-driven flows in the channel between two major lagoons [Figs. 9(d and e)].

Nonhydrostatic Processes

The prescribed vertical flow structure in NEOWAVE enables more realistic descriptions of generation, shoaling, and propagation of tsunamis. Fig. 14 compares the hydrostatic and nonhydrostatic solutions to highlight the role of these processes in defining the wave amplitude across the ocean. The near-field computation off northeast Japan covers an elapsed time of 10 hours to capture resonance oscillations over the continental shelf and slope complex (Yamazaki et al. 2013). The slip distribution, as shown in Fig. 10, contains a wide range of spatial features beneath the wedge and ocean of varying depth. The 24-arcsec (720-m) grid resolves source and wave processes over the margin for computation of the maximum sea-surface elevations, shown in Figs. 14(a and b), with and without nonhydrostatic effects. Having the same final seafloor deformation, the nonhydrostatic model also include the rupture sequence, spreading of the excitation over the water column, and inertia of the subsequent sea-surface descent or upswing. These source processes, along with local dispersion [Eq. (3)] and period-dependent shoaling [Eq. (20)] over the continental slope, provide a more complete account of the tsunami waves approaching the coast to serve as a reference for comparison with the hydrostatic solution.

The static initial sea-surface condition mirrors the final seafloor deformation with fine local bathymetric features unfiltered by the water column (Fig. 10). The hydrostatic approach gives slightly higher initial sea-surface pulses at the epicentral and adjacent near-trench uplift patches by 5% and 7%, but overestimates the wave amplitude by 24% above the narrow strip of uplift to the northeast along the trench. These values are consistent with the numerical experiment in Fig. 3 and are well within the valid range of the nonhydrostatic model for tsunami generation. A proper account of the shoaling process becomes necessary to avoid unrealistic amplification of short-period noise from the static initial condition over the continental margin. The shallow-water approximation leads to shoaling of all harmonics at the maximum gradient of $\gamma = 1/4$ [Eq. (20)]. Along with the lack of local and frequency dispersion, Fig. 14(c) shows the hydrostatic approach overestimates the incident wave amplitude by 31%–35% near the shelf break along the most severely impacted coast. With all harmonics

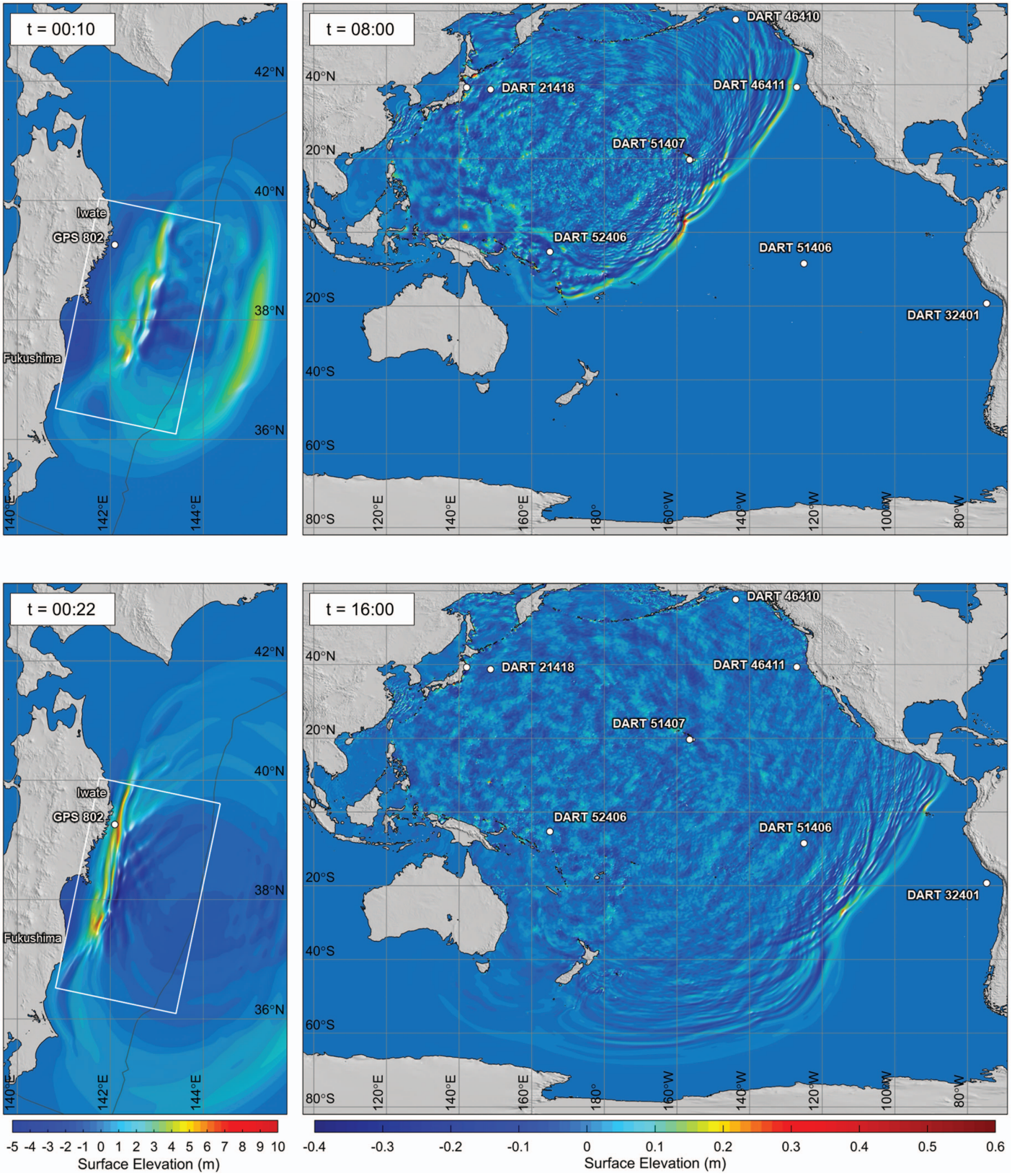

Fig. 11. (Color) Snapshots of computed near and far-field sea-surface elevations for the 2011 Tohoku tsunami at elapsed time (h:min) after earthquake initiation. White rectangle denotes the rupture zone and grey line indicates Japan Trench in the near field. White circles with labels denote water-level stations for signal comparison in Fig. 12. (Background map from GEBCO's gridded dataset.)

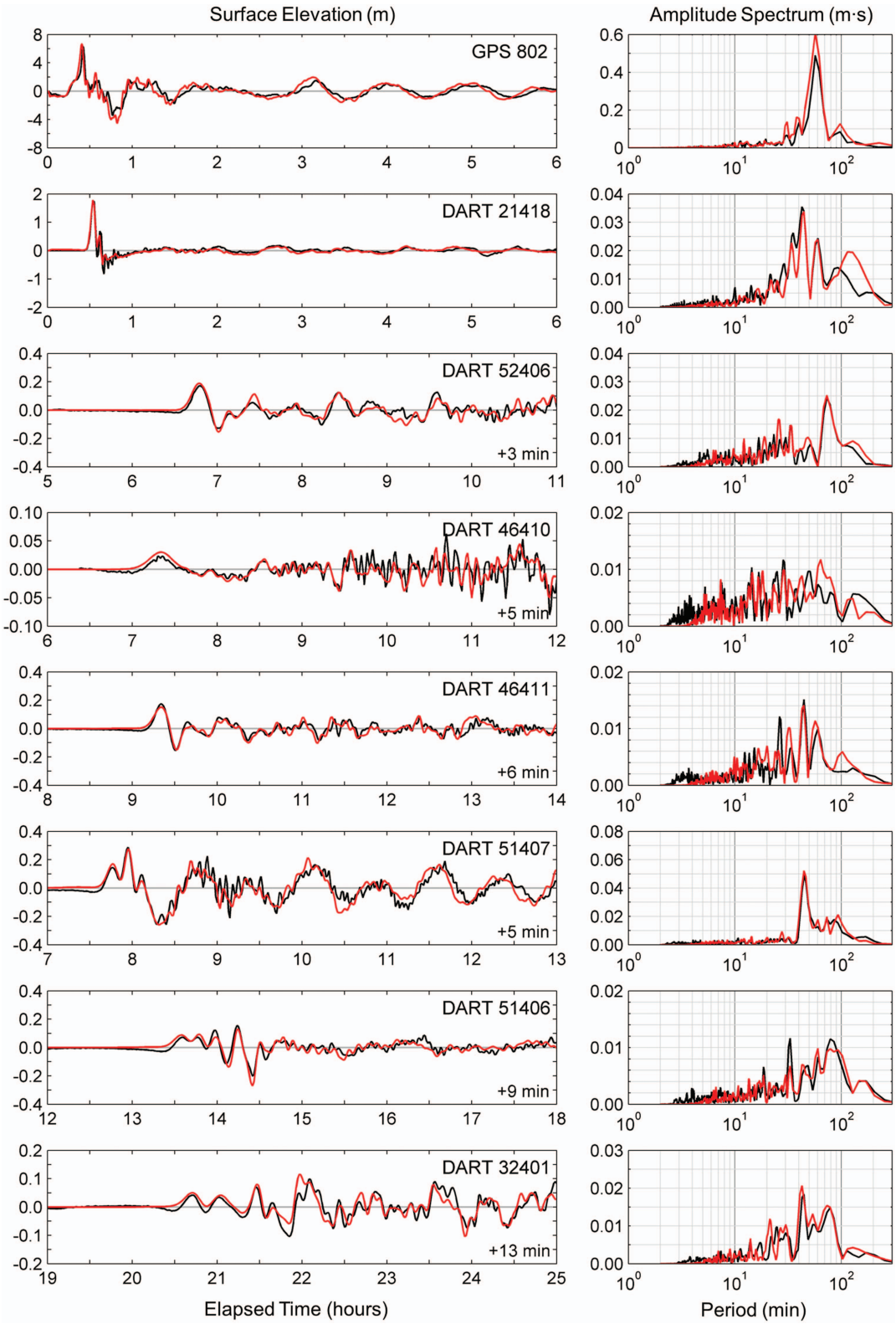

Fig. 12. (Color) Comparison of recorded (black) and computed (red) sea-surface elevations at selected near and far-field offshore water level stations for the 2011 Tohoku tsunami (see Fig. 11 for station locations). The computed waveforms at far-field stations are shifted by the indicated amounts to correct for earth elasticity and water density variation in matching the recorded arrival.

propagating at the same speed, the leading wave amplitude is up to 24% higher immediately offshore of the source region in comparison to the nonhydrostatic solution.

The far-field computation covers a 72-h elapsed time to fully develop resonance oscillations around the Pacific Ocean and in adjacent shallow seas (Bai et al. 2015a). The maximum sea-surface elevation in the open ocean corresponds to the tsunami waves directly from the source. The hydrostatic and nonhydrostatic solutions in Figs. 14(a and b) share the same pattern of main and side lobes associated with the source configuration, as well as the

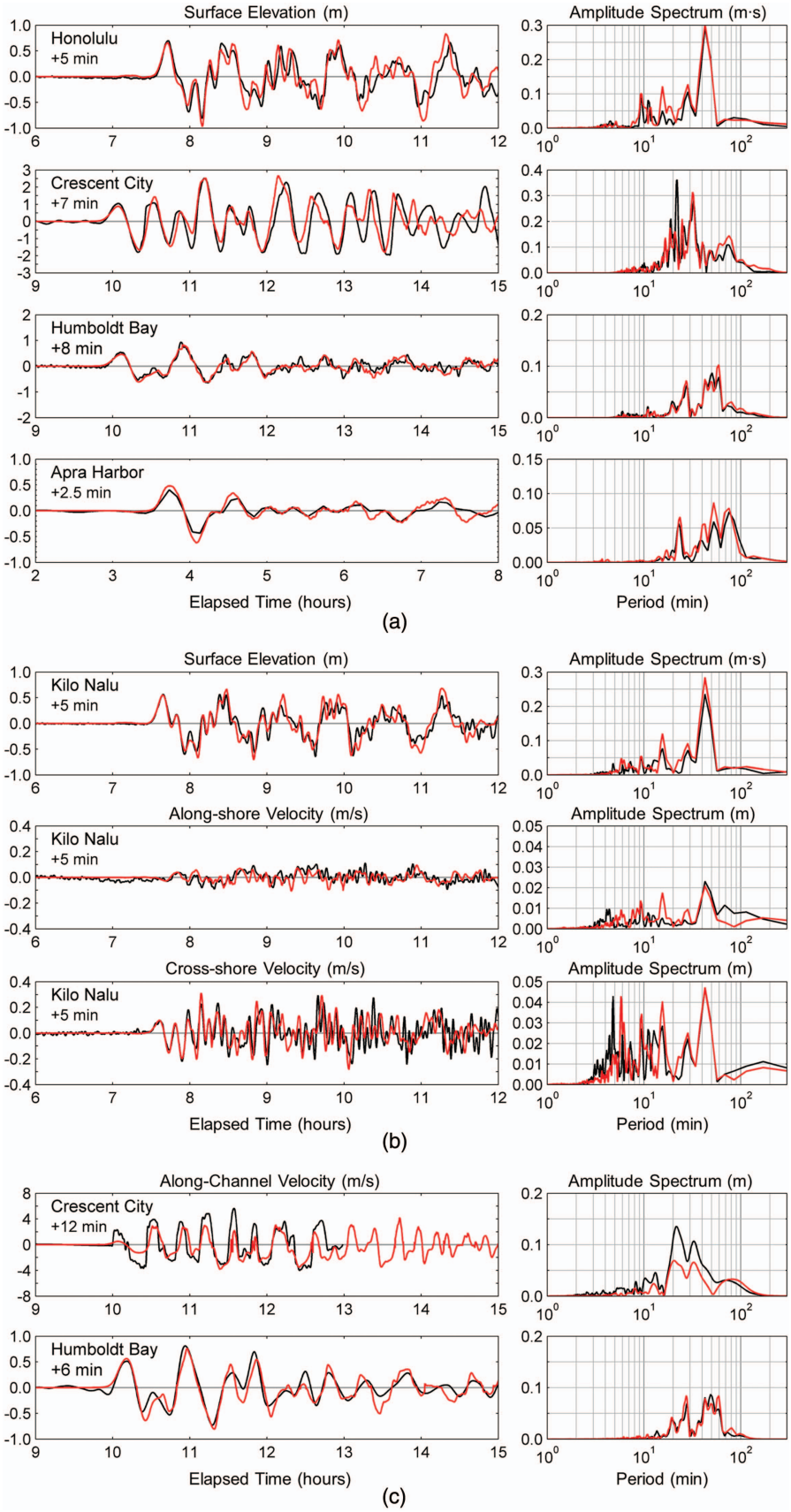

Fig. 13. (Color) Comparison of recorded data (black) with model predictions (red) at coastal stations for the 2011 Tohoku tsunami (see Fig. 9 for locations): (a) harbor tide gauges; (b) kilo Nalu pressure sensor and ADCP outside Honolulu Harbor; and (c) video camera at Crescent City Harbor and ACDP at Humboldt Bay. The time series have 1 min intervals except for the Apra Harbor tide gauge record with 6 min. The recorded and computed currents are depth-averaged except for the video-inferred surface velocity in Crescent City Harbor. The computed time series are shifted by the indicated amounts in matching the recorded arrivals.

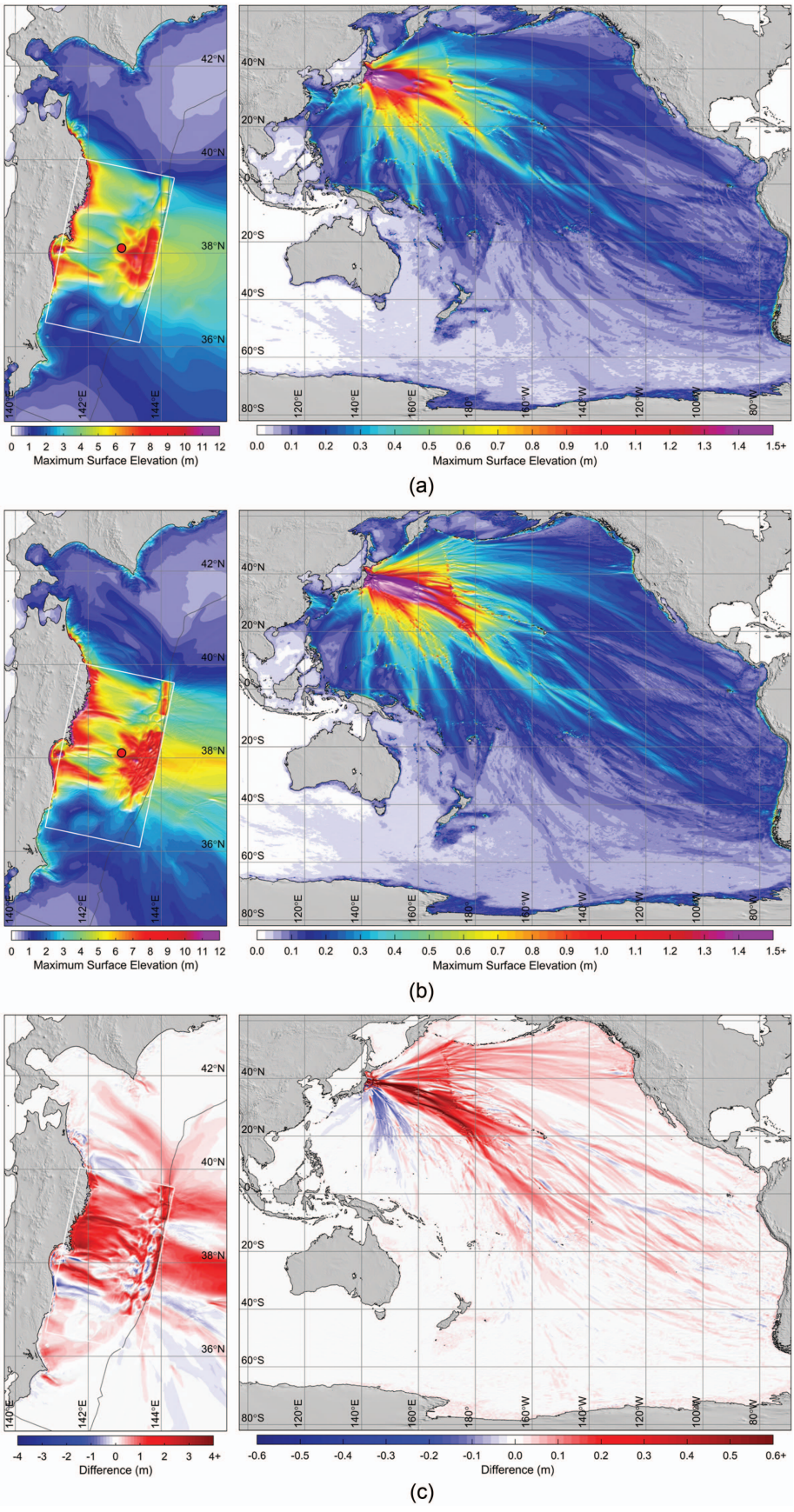

Fig. 14. (Color) Computed maximum sea-surface elevations in the near and far field for the 2011 Tohoku tsunami: (a) nonhydrostatic modeling; (b) hydrostatic modeling; and (c) difference between hydrostatic and nonhydrostatic approaches with positive and negative values indicating higher and lower predictions by the former. White rectangle and red circle denote the rupture model outline and earthquake epicenter in the near field. (Background map from GEBCO's gridded dataset.)

seafloor morphology such as seamounts and island chains, but have noticeably different wave amplitudes across the ocean. The initial long-crested system from the large near-trench slip have a prominent leading wave with a dominant period of 45 min and a series of higher harmonics from the detailed seafloor excitation. Dispersion decreases the wave amplitude most rapidly near the source in the main lobe as the short-period components lag behind the leading wave. The absence of dispersion in the hydrostatic computation results in overestimation of the wave amplitude by up to 39%, as shown in Fig. 14(c). The effects of dispersion are weaker in the side lobes due to dominance of the radial and diffracted waves with longer dominant periods of 60 and 90 min. The hydrostatic and nonhydrostatic solutions are very similar to the south and immediately northeast of the source region.

Discussion and Conclusions

We have demonstrated through mathematical analyses and numerical examples the efficacy of NEOWAVE for modeling quasi three-dimensional tsunami processes across a wide range of spatial and temporal scales. Much of the model versatility derives from complementary properties between the governing equations and numerical schemes. The governing equations involve first-order temporal and spatial derivatives, but implicitly include third-order dispersion and second-order shoaling properties comparable to the Boussinesq-type approach of Peregrine (1967). Parameterization of the vertical velocity and nonhydrostatic pressure with linear profiles leads to slightly weaker dispersion properties in the range of long and intermediate waves that are offset by numerical dispersion from the staggered finite-difference scheme with semi-implicit time integration. Using results from a Navier-Stokes model as a reference, the prescribed vertical flow structure can adequately describe attenuation and spreading of seafloor excitation over the water column for modeling of tsunami generation. In comparison, the dispersion property from the Boussineq-type equations is highly accurate in the tsunami range. The spatial discretization can lead to excess dispersion and lower celerity in the numerical solution, as pointed out early on by Abbott et al. (1984). Baba et al. (2017) encountered such a dilemma in modeling trans-Pacific tsunami propagation with the Boussinesq-type approach and stressed the need to use very small grid spacing to suppress numerical dispersion.

The hydrostatic and nonhydrostatic flow parameters are determined in two steps with the latter used as a correction to complete the solution with three-dimensional effects. A shock-capturing scheme in the hydrostatic step describes breaking waves as flow discontinuities, which are not fully compatible with the nonhydrostatic solution. The issue is resolved by local deactivation and reactivation of the nonhydrostatic correction based on predefined bore formation criteria. This ad hoc approach, which was proven effective at the 2009 NSF inundation model benchmarking workshop, also enables extension of Boussinesq-type models to include shock-capturing capabilities (e.g., Kazolea et al. 2012; Roeber and Cheung 2012; Shi et al. 2012; Tonelli and Petti 2012). The hydrostatic step also utilizes the advective speed from a first-order upwind approximation known to be dissipative, but its effects on transoceanic propagation appear to be negligible, as indicated by the good agreement with both near and far-field measurements from the 2011 Tohoku tsunami case study as well as other modeling work (e.g., Lay et al. 2013; Li et al. 2016b; Bai et al. 2022). The numerical solution remains stable over highly complex reef bathymetry in tropical and subtropical coastal environments. The dissipative property becomes instrumental as numerical viscosity in modeling detailed tsunami-induced flows in harbor and coastal areas. Lynett et al. (2017) concluded from the 2015 NTHMP benchmarking study that such a low-order three-dimensional approach is superior to high-order two-dimensional models based on Boussinesq-type equations in describing shear and separation-driven currents.

The nonhydrostatic step introduces vertical flow dynamics through an implicit Poisson-type solver to more precisely describe generation, dispersion, and shoaling of tsunami waves. The case study of the 2011 Tohoku tsunami demonstrates the capability to resolve leading and trailing waves from the source region to far-flung shores in sheltered waters across the Pacific Ocean. A hydrostatic model does not necessarily provide more conservative predictions of coastal inundation and current for practical application just because the lack of dispersion results in larger leading wave amplitudes offshore. Continental and insular shelves have a tendency to trap wave energy, producing the largest wave at the shore well after the initial arrival, and the response of such dynamic systems also depends on the frequency and phase of the excitation. Although nonlinear wave scattering releases higher harmonics at the coast, these locally-generated short-period waves are not as persistent and effective as those from frequency dispersion in exciting resonance over shallow shelves (Bai and Cheung 2016). The nonhydrostatic approach has gradually received attention due to recognition of higher-order tsunami processes. The governing equations, discretization schemes, and the solution procedures are conducive to a modular code structure in which model features can be added or switched on and off systematically for specific applications. Existing nonlinear shallow-water models can be augmented to include a Poisson-type solver for nonhydrostatic properties without significant alternation of the original code structure.

Resolution of the space-time evolution of slip during large earthquakes has recently been enhanced by joint analysis of seismic and geodetic observations, but these data provide very limited resolution of slip on shallow plate boundaries far offshore (e.g., Lay 2018). Determining finite-fault models along with forward modeling or inversion of tsunami observations has improved the resolution over the entire fault, especially the shallow slip out near the trench that has the most influence on the resulting tsunami (Cheung et al. 2022). The ability of the nonhydrostatic approach to account for time-varying seafloor deformation provides a seamless connection with finite-fault modeling to enable self-consistent kinematic representations of earthquake rupture (e.g., Bai et al. 2014, 2017, 2022; Li et al. 2016b; Yamazaki et al. 2018; Ye et al. 2021). The quasi three-dimensional process realistically accounts for the seafloor deformation pattern and local water depth to ensure accurate reproduction of the initial sea-surface motion, giving reliable tsunami amplitudes for heterogeneous slip distributions. This is also essential in joint inversion of tsunami, geodetic, and seismic data for slip distributions involving many small subfault responses (e.g., Yue et al. 2015; Li et al. 2016a). The 2011 Tohoku tsunami case study demonstrates considerably different hydrostatic and nonhydrostatic predictions at shelf breaks and immediately off the trench. Any model approximation will inevitably distort the slip distribution and timing to match tsunami observations through forward computation or inversion analysis. The improved capabilities, along with recently available high-resolution coastal bathymetry, provide an opportunity to reanalyze tsunamigenic earthquakes previously inferred from hydrostatic modeling and update the respective source models for improving understanding of megathrust properties (e.g., Yamazaki et al. 2021).

Even though frequency dispersion might have a secondary role in near-field tsunamis, the nonhydrostatic calculations are still

critical for realistic description of coastal impacts, especially for shallow ruptures with slip extending to the trench. The harmonic components from seafloor uplift are not yet fully dispersed over continental or insular slopes. It is important to describe local dispersion and period-dependent shoaling for accurate resolution of the near-shore wave amplitude and phase. This capability is demonstrated by reproduction of the wave transformation across the steep reef slope in the 2009 Benchmark II experiment, as well as the observed onshore and offshore impulsive waves generated by the large near-trench slip of the 2011 Tohoku earthquake. More importantly, the vertical inertia force in the nonhydrostatic system enhances the upswing of the initial sea-surface dropdown from subsidence landward of the uplift. Constructive or destructive interference of subsequent local oscillations with arriving waves generated at different water depths across the continental slope can have strong influence on computed coastal runup (e.g., Yamazaki et al. 2018, 2021). In summary, accurate modeling of tsunami processes and coastal impacts requires a combination of hydrostatic and nonhydrostatic properties accentuated by carefully constructed numerical schemes. The embedded capabilities in NEOWAVE provide an additional level of details and precision in advancing studies of submarine earthquake processes as well as the concomitant tsunami hazards.

Data Availability Statement

Some data, models, or code that support the findings of this study are available from the corresponding author upon reasonable request. These cover models, input files, and output data for production of the figures presented in this paper, but do not include proprietary software and third-party data.

Acknowledgments

The development of NEOWAVE was supported by the University of Hawaii Sea Grant College Program Grant NA05ORA417048 and its benchmarking by the National Tsunami Hazard Mitigation Program Grants NA14NWS4670042 and NA15NWS4670025 via Hawaii Emergency Management Agency. We thank Juan Horrillo for providing the Navier-Stokes model results of tsunami generation, Amanda Admire for the current data at Crescent City Harbor and Humboldt Bay, and Patrick Lynett for the laboratory measurements used in the 2009 NSF and 2015 NTHMP benchmarking workshops. SOEST Contribution No. 11618.

References

Abbott, M. B., A. D. McCowan, and I. R. Warren. 1984. "Accuracy of short-wave numerical models." *J. Hydraul. Eng.* 110 (10): 1287–1301. https://doi.org/10.1061/(ASCE)0733-9429(1984)110:10(1287).

Admire, A. R., L. A. Dengler, G. B. Crawford, B. U. Uslu, J. C. Borrero, S. D. Greer, and R. I. Wilson. 2014. "Observed and modeled currents from the Tohoku-oki, Japan and other recent tsunamis in Northern California." *Pure Appl. Geophys.* 171 (12): 3385–3403. https://doi.org/10.1007/s00024-014-0797-8.

Baba, T., S. Allgeyer, J. Hossen, P. R. Cummins, H. Tsushima, K. Imai, K. Yamashita, and T. Kato. 2017. "Accurate numerical simulation of the far-field tsunami caused by the 2011 Tohoku earthquake, including the effects of Boussinesq dispersion, seawater density stratification, elastic loading, and gravitational potential change." *Ocean Modell.* 111 (Mar): 46–54. https://doi.org/10.1016/j.ocemod.2017.01.002.

Bai, Y., and K. F. Cheung. 2013. "Dispersion and nonlinearity of multi-layer non-hydrostatic free-surface flow." *J. Fluid Mech.* 726 (Jul): 226–260. https://doi.org/10.1017/jfm.2013.213.

Bai, Y., and K. F. Cheung. 2016. "Hydrostatic versus non-hydrostatic modeling of tsunamis with implications for insular shelf and reef environments." *Coastal Eng.* 117 (Nov): 32–43. https://doi.org/10.1016/j.coastaleng.2016.07.008.

Bai, Y., and K. F. Cheung. 2018. "Linear shoaling of free-surface waves in multi-layer non-hydrostatic models" *Ocean Modell.* 121 (Jan): 90–104. https://doi.org/10.1016/j.ocemod.2017.11.005.

Bai, Y., K. F. Cheung, Y. Yamazaki, T. Lay, and L. Ye. 2014. "Tsunami surges around the Hawaiian Islands from the 1 April 2014 North Chile Mw 8.1 earthquake." *Geophys. Res. Lett.* 41 (23): 8512–8521. https://doi.org/10.1002/2014GL061686.

Bai, Y., T. Lay, K. F. Cheung, and L. Ye. 2017. "Two regions of seafloor deformation generated the tsunami for the 13 November 2016, Kaikoura, New Zealand earthquake." *Geophys. Res. Lett.* 44 (13): 6597–6606. https://doi.org/10.1002/2017GL073717.

Bai, Y., C. Liu, T. Lay, K. F. Cheung, and L. Ye. 2022. "Optimizing a model of coseismic rupture for the 22 July 2022 M_w 7.8 Simeonof earthquake by exploiting acute sensitivity of tsunami excitation across the shelf break." *J. Geophys. Res. Solid Earth* 127 (7): e2022JB024484. https://doi.org/10.1029/2022JB024484.

Bai, Y., Y. Yamazaki, and K. F. Cheung. 2015a. "Interconnection of multi-scale standing waves across the Pacific Basin from the 2011 Tohoku tsunami." *Ocean Modell.* 92 (Jun): 183–197. https://doi.org/10.1016/j.ocemod.2015.05.005.

Bai, Y., Y. Yamazaki, and K. F. Cheung. 2015b. "NEOWAVE." In *Proc., Results of the 2015 National Tsunami Hazard Mitigation Program Model Benchmarking Workshop*, 165–177. Silver Spring, MD: National Weather Service.

Bai, Y., Y. Yamazaki, and K. F. Cheung. 2018. "Convergence of multilayer nonhydrostatic models in relation to Boussinesq-type equations." *J. Waterw. Port Coastal Ocean Eng.* 144 (2): 06018001. https://doi.org/10.1061/(ASCE)WW.1943-5460.0000438.

Bletery, Q., A. Sladen, B. Delouis, M. Vallée, J. M. Nocquet, L. Rolland, and J. Jiang. 2014. "A detailed source model for the M_w 9.0 Tohoku-Oki earthquake reconciling geodesy, seismology, and tsunami records." *J. Geophys. Res. Solid Earth* 119 (10): 7636–7653. https://doi.org/10.1002/2014JB011261.

Bricker, J. D., S. Munger, C. Pequignet, J. R. Wells, G. Pawlak, and K. F. Cheung. 2007. "ADCP observations of edge waves off Oahu in the wake of the November 2006 Kuril Islands tsunami." *Geophys. Res. Lett.* 34 (23): L23617. https://doi.org/10.1029/2007GL032015.

Casulli, V. 1990. "Semi-implicit finite difference methods for the two-dimensional shallow water equations." *J. Comput. Phys.* 86 (1): 56–74. https://doi.org/10.1016/0021-9991(90)90091-E.

Casulli, V., and G. Stelling. 1998. "Numerical simulation of 3D quasi-hydrostatic, free surface flows." *J. Hydraul. Eng.* 124 (7): 678–686. https://doi.org/10.1061/(ASCE)0733-9429(1998)124:7(678).

Catalán, P. A., et al. 2015. "The 1 April 2014 Pisagua tsunami: Observations and modeling." *Geophys. Res. Lett.* 42 (8): 2918–2925. https://doi.org/10.1002/2015GL063333.

Cheung, K. F., Y. Bai, and Y. Yamazaki. 2013. "Surges around the Hawaiian Islands from the 2011 Tohoku tsunami." *J. Geophys. Res. Oceans* 118 (10): 5703–5719. https://doi.org/10.1002/jgrc.20413.

Cheung, K. F., T. Lay, L. Sun, and K. Yamazaki. 2022. "Tsunami size variability with rupture depth." *Nat. Geosci.* 15 (1): 33–36. https://doi.org/10.1038/s41561-021-00869-z.

Cheung, K. F., Y. Wei, Y. Yamazaki, and S. C. Yim. 2011. "Modeling of 500-year tsunamis for probabilistic design of coastal infrastructure in the Pacific Northwest." *Coastal Eng.* 58 (10): 970–985. https://doi.org/10.1016/j.coastaleng.2011.05.003.

Drikakis, D., and P. K. Smolarkiewicz. 2001. "On spurious vortical structures." *J. Comput. Phys.* 172 (1): 309–325. https://doi.org/10.1006/jcph.2001.6825.

Harten, A. 1983. "High resolution schemes for hyperbolic conservation laws." *J. Comput. Phys.* 49 (3): 357–393. https://doi.org/10.1016/0021-9991(83)90136-5.

Hayes, G. P., D. J. Wald, and R. L. Johnson. 2012. "Slab 1.0: A three-dimensional model of global subduction zone geometries." *J. Geophys. Res. Solid Earth* 117 (1): B01302. https://doi.org/10.1029/2011JB008524.

Horrillo, J. 2006. "Numerical method for tsunami calculation using full Navier-Stokes equations and the volume of fluid method." Ph. D. thesis, Dept. of Oceanography, Univ. of Alaska.

Horrillo, J., Z. Kowalik, and Y. Shigihara. 2006. "Wave dispersion study in the Indian Ocean-Tsunami of December 26, 2004." *Mar. Geod.* 29 (3): 149–166. https://doi.org/10.1080/01490410600939140.

Imamura, F., N. Shuto, and C. Goto. 1988. "Numerical simulations of the transoceanic propagation of tsunamis." In *Proc., 6th Congress of the Asian and Pacific Regional Division*. Kyoto, Japan: Association of Hydraulic Research.

Jeschke, A., G. K. Pedersen, S. Vater, and J. Behrens. 2017. "Depth-averaged non-hydrostatic extension for shallow water equations with quadratic vertical pressure profile: Equivalence to Boussinesq-type equations." *Int. J. Numer. Methods Fluids* 84 (10): 569–583. https://doi.org/10.1002/fld.4361.

Kajiura, K. 1963. "The leading wave of a tsunami." *Bull. Earthquake Res. Inst.* 41 (3): 535–571.

Kazolea, M., A. I. Delic, I. K. Nikolos, and C. E. Synolakis. 2012. "An unstructured finite volume numerical scheme for extended 2D Boussinesq-type equations." *Coastal Eng.* 69 (Nov): 42–66. https://doi.org/10.1016/j.coastaleng.2012.05.008.

Kirby, J. T., F. Shi, B. Tehranirad, J. C. Harris, and S. T. Grilli. 2013. "Dispersive tsunami waves in the ocean: Model equations and sensitivity to dispersion and Coriolis effects." *Ocean Modell.* 62 (Feb): 39–55. https://doi.org/10.1016/j.ocemod.2012.11.009.

Kowalik, Z., and T. S. Murty. 1993a. *Numerical modeling of ocean dynamics*. Singapore: World Scientific.

Kowalik, Z., and T. S. Murty. 1993b. "Numerical simulation of two-dimensional tsunami runup." *Mar. Geod.* 16 (2): 87–100. https://doi.org/10.1080/15210609309379681.

Lay, T. 2018. "A review of the rupture characteristics of the 2011 Tohoku-oki MwW 9.1 earthquake." *Tectonophysics* 733 (May): 4–36. https://doi.org/10.1016/j.tecto.2017.09.022.

Lay, T., L. Ye, H. Kanamori, Y. Yamazaki, K. F. Cheung, K. Kwong, and K. D. Koper. 2013. "The October 28, 2012 M_w 7.8 Haida Gwaii underthrusting earthquake and tsunami: Slip partitioning along the Queen Charlotte Fault transpressional plate boundary." *Earth Planet. Sci. Lett.* 375 (Aug): 57–70. https://doi.org/10.1016/j.epsl.2013.05.005.

LeVeque, R. J., D. L. George, and M. J. Berger. 2011. "Tsunami modelling with adaptively refined finite volume methods." *Acta Numer.* 20 (5): 211–289. https://doi.org/10.1017/S0962492911000043.

Li, L., and K. F. Cheung. 2019. "Numerical dispersion in non-hydrostatic modeling of long-wave propagation." *Ocean Modell.* 138 (Jun): 68–87. https://doi.org/10.1016/j.ocemod.2019.05.002.

Li, L., K. F. Cheung, H. Yue, T. Lay, and Y. Bai. 2016a. "Effects of dispersion in tsunami Green's functions and implications for joint inversion with seismic and geodetic data: A case study of the 2010 Mentawai M_W 7.8 earthquake." *Geophys. Res. Lett.* 43 (21): 182–191. https://doi.org/10.1002/2016GL070970.

Li, L., T. Lay, K. F. Cheung, and L. Ye. 2016b. "Joint modeling of teleseismic and tsunami wave observations to constrain the 16 September 2015 Illapel, Chile, M^W 8.3 earthquake rupture process." *Geophys. Res. Lett.* 43 (9): 4303–4312. https://doi.org/10.1002/2016GL068674.

Liu, P. L.-F., Y.-S. Cho, M. J. Briggs, U. Kânoğlu, and C. E. Synolakis. 1995. "Runup of solitary waves on a circular island." *J. Fluid Mech.* 302 (Nov): 259–285. https://doi.org/10.1017/S0022112095004095.

Lloyd, P. M., and P. K. Stansby. 1997. "Shallow-water flow around model conical islands of small side slope. II: Submerged." *J. Hydraul. Eng.* 123 (12): 1068–1077. https://doi.org/10.1061/(ASCE)0733-9429(1997)123:12(1068).

Lynett, P. J., et al. 2017. "Inter-model analysis of tsunami-induced coastal currents." *Ocean Modell.* 114 (Jun): 14–32. https://doi.org/10.1016/j.ocemod.2017.04.003.

Lynett, P. J., D. Swigler, H. El Safty, L. Montoya, A. S. Keen, S. Son, and P. Higuera. 2019. "Three-dimensional hydrodynamics associated with a solitary wave traveling over an alongshore variable shallow shelf." *J. Waterw. Port Coastal Ocean Eng.* 145 (6): 04019024. https://doi.org/10.1061/(ASCE)WW.1943-5460.0000525.

Mader, C. L. 2004. *Numerical modeling of water waves*. 2nd ed. Boca Raton, FL: CRC Press.

Madsen, P. A., H. B. Bingham, and H. A. Schäffer. 2003. "Boussinesq-type formulations for fully nonlinear and extremely dispersive water waves: Derivation and analysis." *Proc. R. Soc. London, Ser. A* 459 (2033): 1075–1104. https://doi.org/10.1098/rspa.2002.1067.

Madsen, P. A., D. R. Fuhrman, and B. Wang. 2006. "A Boussinesq-type method for fully nonlinear waves interacting with a rapidly varying bathymetry." *Coastal Eng.* 53 (5–6): 487–504. https://doi.org/10.1016/j.coastaleng.2005.11.002.

Madsen, P. A., R. Murray, and O. R. Sørensen. 1991. "A new form of Boussinesq equations with improved linear dispersion characteristics." *Coastal Eng.* 15 (4): 371–388. https://doi.org/10.1016/0378-3839(91)90017-B.

Madsen, P. A., and O. R. Sørensen. 1992. "A new form of Boussinesq equations with improved linear dispersion characteristics. Part 2: A slowly-varying bathymetry." *Coastal Eng.* 18 (3–4): 183–204. https://doi.org/10.1016/0378-3839(92)90019-Q.

Mori, N., T. Takahashi, T. Yasuda, and H. Yanagisawa. 2011. "Survey of 2011 Tohoku earthquake tsunami inundation and run-up." *Geophys. Res. Lett.* 38 (7): L00G14. https://doi.org/10.1029/2011GL049210.

Nwogu, O. 1993. "Alternative form of Boussinesq equations for nearshore wave propagation." *J. Waterw. Port Coastal Ocean Eng.* 119 (6): 618–638. https://doi.org/10.1061/(ASCE)0733-950X(1993)119:6(618).

Okada, Y. 1985. "Surface deformation due to shear and tensile faults in a half-space." *Bull. Seismol. Soc. Am.* 75 (4): 1135–1154. https://doi.org/10.1785/BSSA0750041135.

Okamoto, T., and D. R. Basco. 2006. "The relative Trough Froude Number for initiation of wave breaking: Theory, experiments and numerical model confirmation." *Coastal Eng.* 53 (8): 675–690. https://doi.org/10.1016/j.coastaleng.2006.02.001.

Peregrine, D. H. 1967. "Long waves on a beach." *J. Fluid Mech.* 27 (9): 815–827. https://doi.org/10.1017/S0022112067002605.

Roeber, V., and K. F. Cheung. 2012. "Boussinesq-type model for energetic breaking waves in fringing reef environments." *Coastal Eng.* 70 (Dec): 1–20. https://doi.org/10.1016/j.coastaleng.2012.06.001.

Saito, T., D. Inazu, T. Miyoshi, and R. Hino. 2014. "Dispersion and nonlinear effects in the 2011 Tohoku-Oki earthquake tsunami." *J. Geophys. Res. Oceans* 119 (8): 5160–5180. https://doi.org/10.1002/2014JC009971.

Saito, T., T. Matsuzawa, K. Obara, and T. Baba. 2010. "Dispersive tsunami of the 2010 Chile earthquake recorded by the high-sampling-rate ocean-bottom pressure gauges." *Geophys. Res. Lett.* 37 (23): L23303. https://doi.org/10.1029/2010GL045290.

Salazar, D., et al. 2022. "Did a 3800-year-old $M_W \sim 9.5$ earthquake trigger major social disruption in the Atacama Desert?" *Sci. Adv.* 8 (14): eabm2996. https://doi.org/10.1126/sciadv.abm2996.

Sato, S., and M. B. Kabiling. 1994. "A numerical simulation of beach evolution based on a nonlinear dispersive wave-current model." In *Proc., 24th Conf. Coastal Engineering*, 2557–2570. Reston, VA: ASCE.

Shi, F., J. T. Kirby, J. C. Harris, J. D. Geiman, and S. T. Grilli. 2012. "A high-order adaptive time stepping TVD solver for Boussinesq modelling of breaking waves and coastal inundation." *Ocean Modell.* 43–44 (Jun): 36–51. https://doi.org/10.1016/j.ocemod.2011.12.004.

Smit, P., T. Janssen, L. Holthuijsen, and J. Smith. 2014. "Non-hydrostatic modeling of surf zone wave dynamics." *Coastal Eng.* 83 (Jan): 36–48. https://doi.org/10.1016/j.coastaleng.2013.09.005.

Stelling, G. S., and S. P. A. Duinmeijer. 2003. "A staggered conservative scheme for every Froude number in rapidly varied shallow water flows." *Int. J. Numer. Methods Fluids* 43 (12): 1329–1354. https://doi.org/10.1002/fld.537.

Stelling, G. S., and M. Zijlema. 2003. "An accurate and efficient finite-difference algorithm for non-hydrostatic free-surface flow with application to wave propagation." *Int. J. Numer. Methods Fluids* 43 (1): 1–23. https://doi.org/10.1002/fld.595.

Tanioka, Y., and K. Satake. 1996. "Tsunami generation by horizontal displacement of ocean bottom." *Geophys. Res. Lett.* 23 (8): 861–864. https://doi.org/10.1029/96GL00736.

Titov, V. V., and C. E. Synolakis. 1998. "Numerical modeling of tidal wave runup." *J. Waterw. Port Coastal Ocean Eng.* 124 (4): 157–171. https://doi.org/10.1061/(ASCE)0733-950X(1998)124:4(157).

Tonelli, M., and M. Petti. 2012. "Shock-capturing Boussinesq model for irregular wave propagation." *Coastal Eng.* 61 (Mar): 8–19. https://doi.org/10.1016/j.coastaleng.2011.11.006.

Wei, G., J. T. Kirby, S. T. Grilli, and R. Subramanya. 1995. "A fully nonlinear Boussinesq model for surface waves. Part 1. Highly nonlinear unsteady waves." *J. Fluid Mech.* 294 (13): 71–92. https://doi.org/10.1017/S0022112095002813.

Wei, Y., X. Z. Mao, and K. F. Cheung. 2006. "Well-balanced finite-volume model for long-wave runup." *J. Waterw. Port Coastal Ocean Eng.* 132 (2): 114–124. https://doi.org/10.1061/(ASCE)0733-950X(2006)132:2(114).

Wood, N., J. M. Jones, Y. Yamazaki, K. F. Cheung, J. Brown, J. L. Jones, and N. Abdollahian. 2019. "Population vulnerability to tsunami hazards informed by previous and projected disasters: A case study of American Samoa." *Nat. Hazards* 95 (3): 505–528. https://doi.org/10.1007/s11069-018-3493-7.

Yamazaki, Y., K. F. Cheung, and Z. Kowalik. 2011a. "Depth-integrated, non-hydrostatic model with grid-nesting for tsunami generation, propagation and run-up." *Int. J. Numer. Methods Fluids* 67 (12): 2081–2107. https://doi.org/10.1002/fld.2485.

Yamazaki, Y., K. F. Cheung, Z. Kowalik, T. Lay, and G. Pawlak. 2012. "NEOWAVE." In *Proc., Results of the NTHMP Model Benchmarking Workshop*, 239–302. Silver Spring, MD: National Weather Service.

Yamazaki, Y., K. F. Cheung, and T. Lay. 2013. "Modeling of the 2011 Tohoku near-field tsunami from finite-fault inversion of seismic waves." *Bull. Seismol. Soc. Am.* 103 (2B): 1444–1455. https://doi.org/10.1785/0120120103.

Yamazaki, Y., K. F. Cheung, and T. Lay. 2018. "A self-consistent fault slip model for the 2011 Tohoku earthquake and tsunami." *J. Geophys. Res. Solid Earth* 123 (2): 1435–1458. https://doi.org/10.1002/2017JB014749.

Yamazaki, Y., Z. Kowalik, and K. F. Cheung. 2009. "Depth-integrated, non-hydrostatic model for wave breaking and run-up." *Int. J. Numer. Methods Fluids* 61 (5): 473–497. https://doi.org/10.1002/fld.1952.

Yamazaki, Y., T. Lay, and K. F. Cheung. 2021. "A compound faulting model for the 1975 Kalapana, Hawaii, earthquake, landslide, and tsunami." *J. Geophys. Res. Solid Earth* 126 (11): e2021JB022488. https://doi.org/10.1029/2021JB022488.

Yamazaki, Y., T. Lay, K. F. Cheung, H. Yue, and H. Kanamori. 2011b. "Modeling near-field tsunami observations to improve finite-fault slip models for the 11 March 2011 Tohoku earthquake." *Geophys. Res. Lett.* 38 (7): L00G15. https://doi.org/10.1029/2011GL049130.

Ye, L., T. Lay, H. Kanamori, Y. Yamazaki, and K. F. Cheung. 2021. "The 22 July 2020 M_W 7.8 Shumagin seismic gap earthquake: Partial rupture of a weakly coupled megathrust." *Earth Planet. Sci. Lett.* 562 (May): 116879. https://doi.org/10.1016/j.epsl.2021.116879.

Yim, S. C., M. J. Olsen, K. F. Cheung, and M. Azadbakht. 2014. "Tsunami modeling, fluid load simulation, and validation using geospatial field data." *J. Struct. Eng.* 140 (8): A4014012. https://doi.org/10.1061/(ASCE)ST.1943-541X.0000940.

Yue, H., T. Lay, L. Li, Y. Yamazaki, K. F. Cheung, L. Rivera, E. M. Hill, K. Sieh, W. Kongko, and A. Muhari. 2015. "Validation of linearity assumptions for using tsunami waveforms in joint inversion of kinematic rupture models: Application to the 2010 Mentawai M_w 7.8 tsunami earthquake." *J. Geophys. Res. Solid Earth* 120 (3): 1728–1747. https://doi.org/10.1002/2014JB011721.

Zijlema, M., G. Stelling, and P. Smit. 2011. "SWASH: An operational public domain code for simulating wave fields and rapidly varied flows in coastal waters." *Coastal Eng.* 58 (10): 992–1012. https://doi.org/10.1016/j.coastaleng.2011.05.015.